Computers and Structures 298 (2024) 107361

Contents lists available at ScienceDirect

Computers and Structures

journal homepage: www.elsevier.com/locate/compstruc

Novel block element with axial-only deformation for limit analysis of masonry arch bridges

Yiwei Hua *, Gabriele Milani

Department of Architecture, Built Environment and Construction Engineering, Politecnico di Milano, Piazza Leonardo da Vinci 32, 20133 Milan, Italy

ARTICLE INFO

Keywords:
Limit analysis
Masonry arch bridges
Arch-fill interaction
Collapse performance
Kinematic theorem

ABSTRACT

This paper proposes a novel limit analysis block element to model the ring behavior in masonry arch bridges, with consideration of axial deformation induced by both bending and axial compressing motions. The governing formulation is established based on the kinematic theorem. After constructing the velocity field of the block element, the new compatibility condition is put forward, followed by a discussion of possible linearization for the element constitutive model. A new heterogeneous limit analysis formulation that accounts for the deformability of the elements is given at the end. For benchmarking purposes, the collapse of an 80-block arch is first investigated to understand the influence of using different constitutive linearizations. Then, the proposed element is applied to analyze the collapse of a practical bridge involving arch-fill interactions. The results indicate a great necessity of considering the deformability of the ring when analyzing the collapse of masonry arch bridges. Compared with previous experimental results of Prestwood Bridge, employing the rigid modeling for the ring will lead to a significantly overestimated load prediction (about 46.3%) while the proposed deformable brick element with quadrilateral-linearized constitutive can produce a very accurate prediction (bias within 1%). Adoption of the hexagon linearization will give rise to a comparatively inflexible block behavior and the corresponding ring performs analogous to the rigid case. Finally, the model proposed gets over the main shortcoming exhibited by a beam discretization of the ring, namely the potential over-flexibility of the bridge arch, induced by the simplification of the actual geometry.

1. Introduction

Being one of the widespread typologies of ancient infrastructure, masonry arch bridges have gained great popularity in both Western and Eastern world due to their high structural efficiency and elegant construction aesthetics. Even now, several of those ancient infrastructures remain in service at a fair load-carrying capacity. However, the presence of cracks or damages, usually caused by long-term exposure to natural circumstances or transportation burdens, may let them take risks when subject to earthquakes, floods, or other extreme conditions. Necessary protective interventions and retrofitting measures should be implemented to further improve their resistance. Before that, however, numerical investigations on the collapse performance of these bridges should be made.

Failure analysis of those bridges is a complicated topic due to the involvement of multiple materials. Besides the stone-like elements (e.g., arch, pile, spandrel, etc.), the backfill on the ring exhibits very different material properties from the stone. The popular commercial package of Finite Element Method (FEM) has difficulties in precisely representing the large deformation or cracking propagation of the soil-like part (e.g. backfill) when analyzing the progressive failure (see [1,2] for instance). Nevertheless, heterogeneous limit analysis has great edges in tackling these aspects. This theoretical framework can conveniently include the velocity discontinuities in the structure and also precisely represent the real bond pattern of the masonry. If the associated flow rules are employed, the governing formulation can be stated as a standard form of Linear Programming (LP). The collapse mechanism and ultimate load of the structure will thus be solved in a quick but robust manner without iterations. This approach has been widely applied to failure analysis of both block systems [3–7] and geotechnical problems [8–12].

The modeling of the masonry arch bridge in heterogeneous limit analysis remains an open question. We can read several contributions that discussed the backfill modeling [13,14] while how to model the arch ring was less concerned since the employment of rigid blocks seems to be a widely accepted solution. This element only takes into account the rigid body motion without the involvement of other deformation-

* Corresponding author.
E-mail addresses: yiwei.hua@polimi.it (Y. Hua), gabriele.milani@polimi.it (G. Milani).

https://doi.org/10.1016/j.compstruc.2024.107361
Received 23 January 2024; Accepted 20 March 2024

induced modes. Such modeling of the masonry has been widely applied to the collapse analysis of walls [15–18], and due to the low-cost description for the block velocity field, it becomes very promising when applied to many large-scale scenes [19–21]. In this paper, however, we will illustrate that such rigid block modeling, may not be reasonable for the arch or vault masonry structure. Actually, we have noticed some indications from the previous literature. As reported by Gilbert et al. [22], using rigid modeling for the ring may bring about an overestimated collapse load prediction. In contrast, Cavicchi and Gambarotta [13,14] introduce deformability into the arch of the Prestwood Bridge and the prediction gets quite close to the on-site test. This indicates that the consideration of the deformability of the brick is important when modeling the ring of masonry arch bridges. The overestimation from using rigid arch modeling could be attributed to the neglect of the axial strain field induced by the compressing and bending motion, and the overall deformation of the ring will thus be significant, which may further lead to a large containment stress produced by the backfill. As a result, the prediction of the load-bearing capacity of the bridge increases. To keep benefit from the high efficiency of rigid elements, several contributions have attempted to reduce these in-element axial deformations to the interfaces between the bricks. However, this simplification may lead to a negative interfacial dilation in the predicted mechanism. The homogenous-deformed element proposed by Sloan [23,24] may also not be an accurate solution for this case where the axial deformation is dominant, as the brick will present homogenous dilation in all directions, again giving rise to an unrealistic mechanism prediction. The beam element proposed by Cavicchi and Gambarotta [13,14] could be a good alternative to deformable modeling of the ring while the beams cannot explicitly account for the thickness of the arch. This may bring unreliable predictions when considering the ring-fill interaction.

Absorbing the innovation of Cavicchi and Gambarotta, this paper proposes a more general solution for the arch ring modeling in the limit analysis of masonry arch bridges: a novel block element with axial deformation only. The governing formulation is established based on the Upper Bound (UB) theory. The organization of the paper is structured as follows: Section 2 first constructs the velocity field of the element induced by compressing and bending motions. Then, constitutive models that describe the deformation of the block are investigated. The corresponding flow rule is assumed as associated. The section will close by giving the new optimization formulation of limit analysis accounting for the deformability. Implementing the proposed elements, in Section 3, we present the collapse analysis of a 2D 80-block with several further parametric studies. In Section 4, a case study of Prestwood Bridge with full consideration of the backfill is carried out, through which we can further understand how the arch ring modeling influences the collapse involving the ring-fill interaction. Section 5 compares the acquired outcomes to the numerical simulation and experiments reported in previous literature. Critical conclusions are finally summarized in Section 6.

2. Methodology

2.1. Geometric compatibility

In this section, we start with constructing the velocity field of this novel element to update the geometric compatibility condition of the upper bound (UB) limit analysis. The velocity field of the block $\mathbf{u}(\mathbf{r})$ can be decomposed into the field induced by the rigid body motion $\mathbf{u}_{\mathscr{R}}(\mathbf{r})$ and the axial deformation $\mathbf{u}_{\mathscr{A}}(\mathbf{r})$. The representation of the rigid body mode is quite straightforward, which can be described through transversal and rotational velocities at the centroid under the global frame (see Fig. 1a). Through the matrix $\mathbf{H}^i_{\mathscr{R}}(\mathbf{r}^i)$, we can obtain the velocity at each point of block E_i, mapped from these centroid unknowns (Eq. (1a)); $\mathbf{r}^i$ denotes the position coordinates of the point relative to the centroid of the element (Eq. (1b)). Columns of $\mathbf{H}^i_{\mathscr{R}}(\mathbf{r}^i)$ collect all the basis functions of the space of rigid body motion $\mathscr{R}$ (as defined in Eq. (2)) over element E_i, corresponding to each centroid component.

$$\mathbf{u}^i_{\mathscr{R}}(\mathbf{r}^i)=\begin{bmatrix}1 & 0 & -(y-\bar{y}^i)\\ 0 & 1 & (x-\bar{x}^i)\end{bmatrix}\begin{bmatrix}u^i\\ v^i\\ \omega^i\end{bmatrix}=\mathbf{H}^i_{\mathscr{R}}(\mathbf{r}^i)\mathbf{u}^i \tag{1a}$$

$$\boldsymbol{r}^i:=[x-\bar{x}^i \quad y-\bar{y}^i]^T,\bar{x}^i:=\frac{1}{4}\sum_{k=1}^{4}x^i_k,\bar{y}^i:=\frac{1}{4}\sum_{k=1}^{4}y^i_k \tag{1b}$$

$$\mathscr{R}(E_i):=\left\{\mathbf{r}_0+\mathbf{B}_{\mathrm{AS}}\cdot\mathbf{r}^i:\mathbf{r}_0\in\mathbb{R}^2,\mathbf{B}_{\mathrm{AS}}\in\mathbb{R}^{2\times2},\mathbf{B}^T_{\mathrm{AS}}=-\mathbf{B}_{\mathrm{AS}}\right\} \tag{2}$$

Construction of the axial deformation space of the block element refers to the classical beam theory. Only axial deformation, caused by both axial compression and bending, is allowed in this element (see Fig. 1a). According to the beam theory, these two deformation modes can be described by axial strain ε^i_α and curvature κ^i (Eq. (3a)), through which the axial strain rate and the velocity field in the element E_i can then be given (Eq. (3b)). Note that here, the representation of the given velocity field is under the local frame ($\mathbf{e}_\alpha$, $\mathbf{e}_\beta$), where the axial basis vector $\mathbf{e}_\alpha$ is defined along the midpoint of two block sections. Again, matrix $\mathbf{H}^i_{\mathscr{A}}(\mathbf{r}^i)$ collects all the basis functions of the space of axial deformation mode $\mathscr{A}(E_i)$ (Eq. (3c)). The space of velocity field for the element $\mathscr{V}(E_i)$ is the direct sum of spaces $\mathscr{R}(E_i)$ and $\mathscr{A}(E_i)$. Namely, the velocity field of the element can be regarded as a superposition of rigid body motion and axial deformation mode (Eq. (4)).

$$\varepsilon^i_\alpha(x_\alpha,y_\beta)=\varepsilon^i_\alpha-\kappa^i y_\beta,x_\alpha:=\mathbf{r}^i\cdot\mathbf{e}^i_\alpha,y_\beta:=\mathbf{r}^i\cdot\mathbf{e}^i_\beta \tag{3a}$$

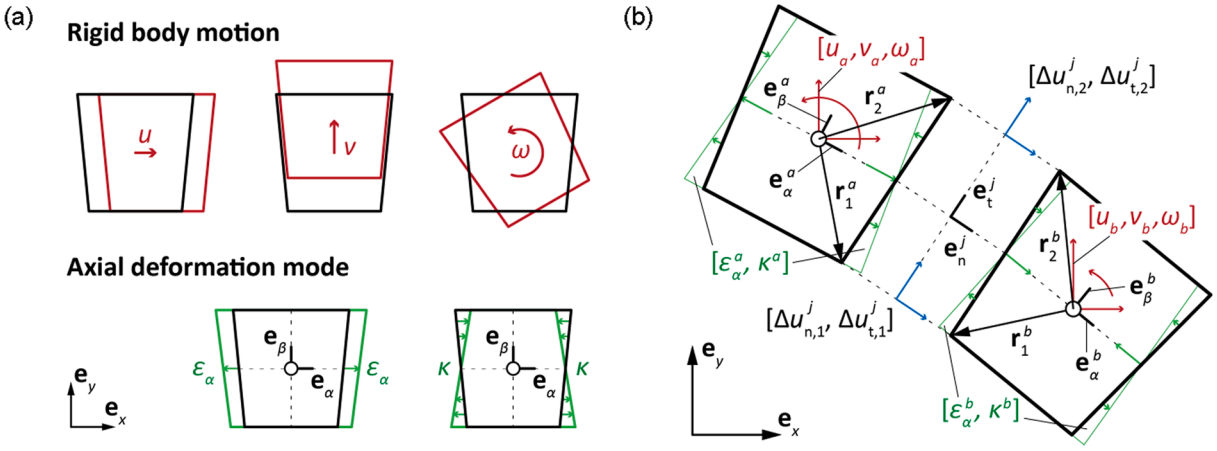

Fig. 1. Axial-only deformable block element: (a) consideration of the element velocity mode; (b) geometric compatibility.

$$u^i_\alpha(x_\alpha, y_\beta) = (\varepsilon^i_\alpha - \kappa^i y_\beta)x_\alpha \Leftrightarrow \mathbf{u}^i_{\mathscr{A}}(\mathbf{r}^i) = \mathbf{H}^i_{\mathscr{A}}(\mathbf{r}^i)\boldsymbol{\varepsilon}^i, \boldsymbol{\varepsilon}^i := \begin{bmatrix} \varepsilon^i_\alpha & \kappa^i \end{bmatrix}^T \tag{3b}$$

$$\mathbf{H}^i_{\mathscr{A}}(\mathbf{r}^i) = \mathbf{e}^i_\alpha \begin{bmatrix} \mathbf{r}^i \cdot \mathbf{e}_\alpha & (\mathbf{r}^i \cdot \mathbf{e}^i_\alpha)(\mathbf{r}^i \cdot \mathbf{e}^i_\beta) \end{bmatrix} \tag{3c}$$

$$\mathbf{u}^i(\mathbf{r}^i) = \mathbf{u}^i_{\mathscr{R}}(\mathbf{r}^i) + \mathbf{u}^i_{\mathscr{A}}(\mathbf{r}^i) = \mathbf{H}^i_{\mathscr{R}}(\mathbf{r}^i)\mathbf{u}^i + \mathbf{H}^i_{\mathscr{A}}(\mathbf{r}^i)\boldsymbol{\varepsilon}^i \tag{4}$$

$$\begin{aligned} \mathbf{q}_j &= \left[\Delta u^j_{\mathrm{n},1}, \Delta u^j_{\mathrm{t},1}, \Delta u^j_{\mathrm{n},2}, \Delta u^j_{\mathrm{t},2}\right]^T = \begin{bmatrix} \mathbf{Q}_j\mathbf{u}^b(\mathbf{r}^b_1) - \mathbf{Q}_j\mathbf{u}^a(\mathbf{r}^a_1) \\ \mathbf{Q}_j\mathbf{u}^b(\mathbf{r}^b_2) - \mathbf{Q}_j\mathbf{u}^a(\mathbf{r}^a_2) \end{bmatrix} \\ &= \begin{bmatrix} -\left(\mathbf{A}^a_{j,u}\right)^T & \left(\mathbf{A}^b_{j,u}\right)^T \end{bmatrix} \begin{bmatrix} \mathbf{u}^a \\ \mathbf{u}^b \end{bmatrix} + \begin{bmatrix} -\left(\mathbf{A}^a_{j,\varepsilon}\right)^T & \left(\mathbf{A}^b_{j,\varepsilon}\right)^T \end{bmatrix} \begin{bmatrix} \boldsymbol{\varepsilon}^a \\ \boldsymbol{\varepsilon}^b \end{bmatrix} \end{aligned} \tag{5a}$$

$$\mathbf{Q}_j = \begin{bmatrix} \mathbf{e}^j_{\mathrm{n}} & \mathbf{e}^j_{\mathrm{t}} \end{bmatrix}^T, \mathbf{A}^i_{j,u} = \begin{bmatrix} \mathbf{Q}_j\mathbf{H}^i_{\mathscr{R}}(\mathbf{r}^i_1) \\ \mathbf{Q}_j\mathbf{H}^i_{\mathscr{R}}(\mathbf{r}^i_2) \end{bmatrix}^T, \mathbf{A}^i_{j,\varepsilon} = \begin{bmatrix} \mathbf{Q}_j\mathbf{H}^i_{\mathscr{A}}(\mathbf{r}^i_1) \\ \mathbf{Q}_j\mathbf{H}^i_{\mathscr{A}}(\mathbf{r}^i_2) \end{bmatrix}^T, i = a, b \tag{5b}$$

After obtaining the velocity field of the element, the interfacial discontinuity is thus computable, collected in vector $\mathbf{q}$. Every specific joint j has 4 degrees of freedom assigned at two interfacial nodes, accounting for the normal and tangential velocity discontinuities of each node (denote as $\Delta u^j_{\mathrm{n},k}$ and $\Delta u^j_{\mathrm{t},k}$, $k = 1$ or 2). Now considering two adjacent blocks a and b (Fig. 1b), the velocity jump for joint j can be calculated through the subtraction of the velocities at the corresponding vertex of the elements (Eq. (5a)). Then we use the rotational matrix $\mathbf{Q}_j$ to project the velocities to the interfacial frame ($\mathbf{e}_{\mathrm{n}}$, $\mathbf{e}_{\mathrm{t}}$) (Eq. (5b)). Assembling this equation over all the interfaces, the matrix form of the geometric compatibility condition can be written as Eq. (6). Compared with the formulation of classical rigid block limit analysis [25,26], the new compatibility condition supplements a term of the velocity contributed by the element deformation.

$$\mathbf{A}^T_u\mathbf{u} + \mathbf{A}^T_\varepsilon\boldsymbol{\varepsilon} = \mathbf{q} \tag{6}$$

2.2. Constitutive model and flow rule

Then, we proceed to investigate the constitutive model and flow rule for the interfacial discontinuities and supplemented in-element strain components. Regarding the ones for the interfaces, we use the classic Mohr-Coulomb friction model (Eq. (7)), illustrated in Fig. 2), which is an established solution accepted by the scientific community (see [21,25,26,6]). Matrix representative of this constitutive relation is given in Eq. (8a). Here, $\mathbf{x}$ denotes the vector of interfacial resultants (Eq. (8c)).

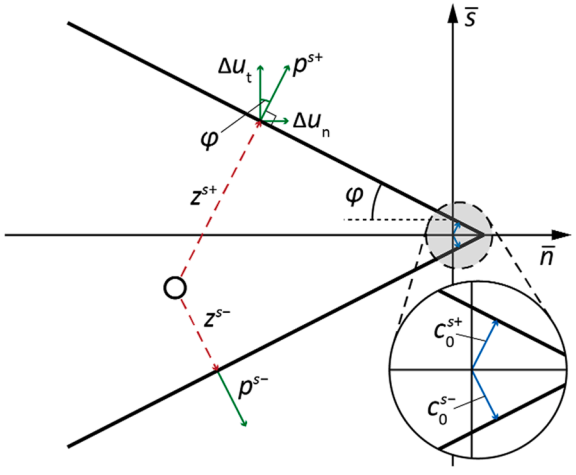

Fig. 2. Interfacial constitutive model: Mohr-Coulomb friction model, associated flow rule.

For each joint j, it contains the normal and tangential resultant forces applied at two interfacial nodes. $\mathbf{z}_0$ is the slack variable (Eq. (8c)), whose components indicate the orthogonal distance from the current force state to each limit surface (as illustrated in Fig. 2). The value is negative if the current force state is in the limit domain. As Mohr-Coulomb relation needs to be applied to two pairs of nodal resultants, for each interface, we require four slack variables in total and all of them should be non-positive. The cohesion force vector $\mathbf{c}_0$ and constitutive operator $\mathbf{N}$ for specific joint j are given in Eqs. (8b) and (8d) (see [25,26] for details). Remark that the components of $\mathbf{c}_0$ are the effective nodal cohesion force for each node, which can be computed from the integral of interface cohesion c_0 on half of the section. On the kinematic side, we adopt the associated flow rule to correlate the unknown velocity jumps $\mathbf{q}$ and plastic multipliers $\mathbf{p}$ (Eq. (9)). Due to the associativity, the mapping operator for the flow rule is the transpose of the one in the constitutive law (see Eq. (10a)). It is also worthwhile to remark on the complementary property of slack variable $\mathbf{z}_0$ from the static side and plastic multipliers $\mathbf{p}$ from the kinematic side (defined in Eq. (10b)). In fact, a static force state must imply zero plastic flow at the interfaces and vice versa. Therefore, for each pair of slack variable and plastic multiplier, only one can be non-zero, i.e. $\mathbf{z}^T_0\mathbf{p} = \mathbf{0}$ (complementary property). The dissipation at the interfaces is defined as the inner dot of interfacial resultant $\mathbf{x}$ and velocity jump vector $\mathbf{q}$. Applying Eqs. (8a) and (10a) as well as considering the complementary property of $\mathbf{z}_0$ and $\mathbf{p}$, it can be represented by the cohesion force vector $\mathbf{c}_0$ and the plastic multiplier $\mathbf{p}$ (Eq. (11)).

$$F(\bar{n}, \bar{s}) = \bar{n}\sin\varphi + |\bar{s}|\cos\varphi - \frac{1}{2}c_0 A\cos\varphi \leqslant 0 \tag{7}$$

$$\mathbf{N}\mathbf{x} - \mathbf{z}_0 = \mathbf{c}_0, \mathbf{z}_0 \leqslant \mathbf{0} \tag{8a}$$

$$\mathbf{N}_j = \begin{bmatrix} \sin\varphi_j & \cos\varphi_j & & \\ \sin\varphi_j & -\cos\varphi_j & & \\ & & \sin\varphi_j & \cos\varphi_j \\ & & \sin\varphi_j & -\cos\varphi_j \end{bmatrix} \tag{8b}$$

$$\mathbf{x}_j := \begin{bmatrix} \bar{n}^j_1 & \bar{s}^j_1 & \bar{n}^j_2 & \bar{s}^j_2 \end{bmatrix}^T, \mathbf{z}_{0,j} := \begin{bmatrix} z^{s+}_{1,j} & z^{s-}_{1,j} & z^{s+}_{2,j} & z^{s-}_{2,j} \end{bmatrix}^T \tag{8c}$$

$$\mathbf{c}_{0,j} := \begin{bmatrix} c^{s+}_{0,j} & c^{s-}_{0,j} & c^{s+}_{0,j} & c^{s-}_{0,j} \end{bmatrix}^T, c^{s+}_{0,j} = c^{s-}_{0,j} = \frac{1}{2}c_{0,j}A_j\cos\varphi_j \tag{8d}$$

$$\Delta u_{\mathrm{n},k} = p^{s+}_k\sin\varphi + p^{s-}_k\sin\varphi, \Delta u_{\mathrm{t},k} = p^{s+}_k\cos\varphi - p^{s-}_k\cos\varphi, (k = 1, 2) \tag{9}$$

$$\mathbf{N}^T\mathbf{p} = \mathbf{q}, \mathbf{p} \geqslant \mathbf{0} \tag{10a}$$

$$\mathbf{p}_j := \begin{bmatrix} p^{s+}_{1,j} & p^{s-}_{1,j} & p^{s+}_{2,j} & p^{s-}_{2,j} \end{bmatrix}^T \tag{10b}$$

$$P^C_D := \mathbf{x}^T\mathbf{q} = \mathbf{x}^T\mathbf{N}^T\mathbf{p} = \mathbf{c}^T_0\mathbf{p} + \mathbf{z}^T_0\mathbf{p} = \mathbf{c}^T_0\mathbf{p} \tag{11}$$

The constitutive relation and flow rule for the supplemented in-element variables are established again referring to the beam theory. Following the assumed velocity field in Eq. (3b), the distribution of the strain rate is linear along the height of the section (Eq. (12a)), which can be decomposed into uniform (due to axial force) and centrosymmetric-linear (due to bending) distributions (Fig. 3a). Correspondingly, the stress distributions for the two deformation modes are thus uniform and centrosymmetric-uniform, respectively (Eq. (12b)). Here in the constitutive relation, we introduce the generalized axial force $\widetilde{N}$ and moment $\widetilde{M}$ for the sake of being energy conjugation with the employed deformation variables ε_α and κ. b, h and d are the width, height and depth of the block element, respectively, and W and A represent the plastic modulus and the area of the section.

$$\varepsilon(y_\beta) = \varepsilon_\alpha - \kappa y_\beta \tag{12a}$$

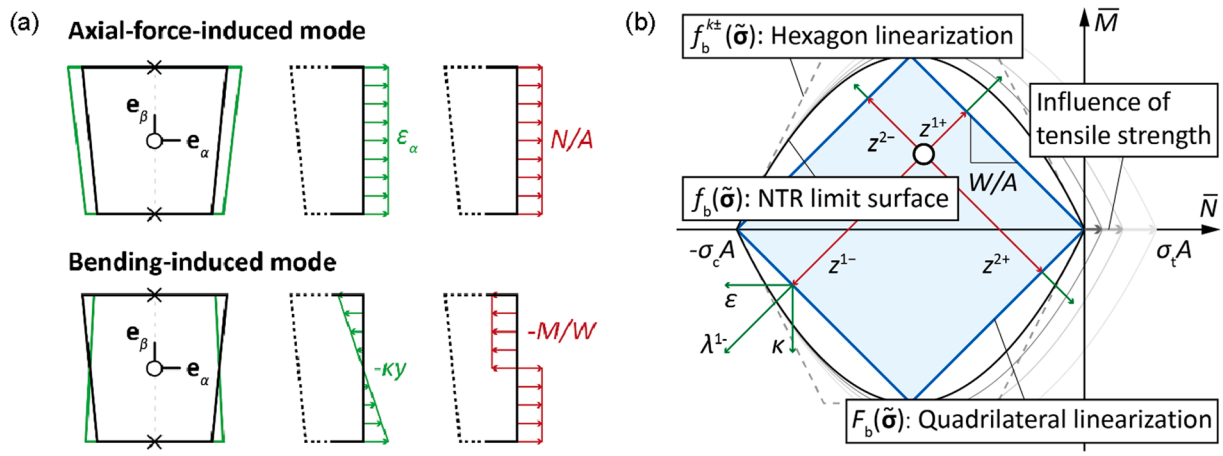

Fig. 3. Constitutive model of the block element: (a) sectional strain and stress distribution; (b) comparison of real NTR limit surface (17), quadrilateral linearization (13), and hexagon linearization (18).

$$\sigma(y_\beta)=\begin{cases}\dfrac{\widetilde{N}}{Ab}-\dfrac{\widetilde{M}}{Wb}, y_\beta\in[0,h/2]\\ \dfrac{\widetilde{N}}{Ab}+\dfrac{\widetilde{M}}{Wb}, y_\beta\in[-h/2,\ 0]\end{cases} \tag{12b}$$

$$\widetilde{N}:=Nb,\widetilde{M}:=Mb,W=\frac{h^2d}{4},A=hd$$

$$F_b\left(\widetilde{N},\widetilde{M}\right)=\begin{cases}\dfrac{\widetilde{N}}{Ab}+\left|\dfrac{\widetilde{M}}{Wb}\right|-\sigma_t\leqslant 0\\ -\dfrac{\widetilde{N}}{Ab}+\left|\dfrac{\widetilde{M}}{Wb}\right|-\sigma_c\leqslant 0\end{cases} \tag{13}$$

We check the stress at the top and bottom surface of the blocks being in the range of tensile strength σ_t and compressive strength σ_c (Fig. 3a). The constitutive constraint can be expressed as Eq. (13), which can also be written as a linear matrix constraint Eq. (14a). Components of the operator $\mathbf{M}$ for specific element i are given in Eq. (14b), where $\tilde{\boldsymbol{\sigma}}$ collects the generalized internal forces of all the elements. $\mathbf{c}_1$ here contains the tensile and compressive strength of the brick material (Eq. (14c)). $\mathbf{z}_1$ is the corresponding slack variable with a similar definition to the interfacial constitutive model (see Eq. (8b)). Graphically, the region of the static-allowed force state defined by the constitutive law Eq. (13) is quadrilateral (blue region in Fig. 3b). Corresponding associated flow constraint can be expressed through the same matrix form Eq. (15a), using the mapping operator that is the transpose of constitutive operator $\mathbf{M}$.

$$\mathbf{M}\tilde{\boldsymbol{\sigma}}-\mathbf{z}_1=\mathbf{c}_1 \tag{14a}$$

$$\mathbf{M}_i=\begin{bmatrix}\dfrac{1}{A_ib_i} & -\dfrac{1}{A_ib_i} & \dfrac{1}{A_ib_i} & -\dfrac{1}{A_ib_i}\\ -\dfrac{1}{W_ib_i} & \dfrac{1}{W_ib_i} & \dfrac{1}{W_ib_i} & -\dfrac{1}{W_ib_i}\end{bmatrix}^T,\tilde{\boldsymbol{\sigma}}_i:=\begin{bmatrix}\widetilde{N}_i & \widetilde{M}_i\end{bmatrix}^T \tag{14b}$$

$$\mathbf{c}_i:=\begin{bmatrix}\sigma_t & \sigma_c & \sigma_t & \sigma_c\end{bmatrix}^T,\mathbf{z}_i:=\begin{bmatrix}z_i^{1+} & z_i^{1-} & z_i^{2+} & z_i^{2-}\end{bmatrix}^T\geqslant\mathbf{0} \tag{14c}$$

$$\mathbf{M}^T\boldsymbol{\lambda}=\boldsymbol{\varepsilon} \tag{15a}$$

$$\boldsymbol{\lambda}_i:=\begin{bmatrix}\lambda_i^{1+} & \lambda_i^{1-} & \lambda_i^{2+} & \lambda_i^{2-}\end{bmatrix}^T\geqslant\mathbf{0} \tag{15b}$$

The dissipation in the element can be computed through the integral strain energy density over the element volume (Eq. (16)), which is equal to the inner dot of the conjugate stress and strain vector defined in Eqs. (14b) and (3b). Applying the constitutive and flow relations (Eqs. (14a) and (15a)), it can be transformed into an expression with only variables from the kinematic side (cohesion $\mathbf{c}_1$ and plastic multiplier vector $\boldsymbol{\lambda}$, defined in Eqs. (14c) and (15b)). Note that all these constraints for the constitutive and flow rules as well as the expression of the dissipation present a very analogous form to the counterparts for the interfaces (compare Eqs. (14a) and (15a)) to Eqs. (8a) and (10a)).

$$\begin{aligned}P_D^{\mathrm{E}} &= \sum_{i=1}^{N_\mathrm{E}}\int_V\sigma^i(y_\beta)\varepsilon^i(y_\beta)dV\\ &= d\sum_{i=1}^{N_\mathrm{E}}b_i\left(\int_0^{h_i/2}\left(\frac{\widetilde{N}_i}{A_ib_i}-\frac{\widetilde{M}_i}{W_ib_i}\right)\left(\varepsilon_\alpha^i-\kappa^iy_\beta\right)+\int_{-h_i/2}^0\left(\frac{\widetilde{N}_i}{A_ib_i}+\frac{\widetilde{M}_i}{W_ib_i}\right)\left(\varepsilon_\alpha^i-\kappa^iy_\beta\right)\right)dy_\beta\\ &= \sum_{i=1}^{N_\mathrm{E}}\widetilde{N}_i\varepsilon_\alpha^i+\widetilde{M}_i\kappa^i=\tilde{\boldsymbol{\sigma}}^T\boldsymbol{\varepsilon}=\tilde{\boldsymbol{\sigma}}^T\mathbf{M}^T\boldsymbol{\lambda}=\mathbf{c}_1^T\boldsymbol{\lambda}\end{aligned} \tag{16}$$

In the aforementioned contribution of Cavicchi and Gambarotta [14], the constitutive model for the beam element is also applicable to the proposed block element, which could be another optional modeling of the deformable ring. The basic idea is to linearize the limit domain of non-tensile resistant (NTR) material. The standard limit domain for the NTR material is bounded by the quadratic curves (see black curves in Fig. 3b, Eq. (17)), and the optimization problem will no longer be a Linear Programming (LP) once including this constraint. To avoid this,

the linearization technique was employed to approximate the curve boundaries into polylines (Eq. (18)). The constraint can then be written as a linear matrix form that is consistent with Eqs. (14a) and (15a). Eq. (19) gives the **M** matrix and **c** vector for specific block i when the linearization precision p_b is set as 6. In this case, the real quadratic limits for NTR material are approximated by a hexagon boundary (dash lines in Fig. 3b).

$$f_b\left(\widetilde{N},\widetilde{M}\right)=\frac{\left|\widetilde{M}\right|}{Wb\sigma_c}+\frac{2\widetilde{N}}{Ab\sigma_c}\left(1+\frac{\widetilde{N}}{Ab\sigma_c}\right)\leqslant 0 \tag{17}$$

$$f_b^{k\pm}\left(\widetilde{N},\widetilde{M}\right)=\pm\frac{\widetilde{M}}{Wb}+\frac{\widetilde{N}}{Ab}\frac{2(p_b+2-4k)}{(p_b-2)}-\frac{8(k-1)^2}{(p_b-2)^2}\sigma_c\leqslant 0, k=1,2,\ldots,\frac{p_b}{2} \tag{18}$$

$$\mathbf{M}_i^*=\begin{bmatrix}\frac{2}{A_ib_i} & 0 & -\frac{2}{A_ib_i} & \frac{2}{A_ib_i} & 0 & -\frac{2}{A_ib_i}\\ \frac{1}{W_ib_i} & \frac{1}{W_ib_i} & \frac{1}{W_ib_i} & -\frac{1}{W_ib_i} & -\frac{1}{W_ib_i} & -\frac{1}{W_ib_i}\end{bmatrix}^T \tag{19}$$

$$\mathbf{c}_i^*=\begin{bmatrix}0 & \frac{\sigma_c}{2} & 2\sigma_c & 0 & \frac{\sigma_c}{2} & 2\sigma_c\end{bmatrix}^T$$

In Fig. 3b, we can note that the linearization proposed in the paper of Cavicchi and Gambarotta [14] circumscribed the actual limit boundary, giving rise to an expansion of the static-allowed domain. Oppositely, the region defined by Eq. (13) proposed in the present paper lies within the quadratic limit domain, which can be understood as a conservative linearization of the NTR constitutive equation. We also plot in Fig. 3b the limit domain with tensile strengths. As indicated by the gray line, the parabolic limit surface will enlarge in proportion when the tensile strength increases. Nevertheless, given that the tensile strength of the brick material is usually quite limited, such expansion of the limit domain can be ignored. Therefore, for the sake of simplicity, we will always assume NTR model for the brick element (i.e. $\sigma_t=0$) in the below analysis. Both quadrilateral (lower-bound-approximated) and hexagon (upper-bound-approximated) linearizations for the constitutive model will be taken into account. The corresponding collapse results of the arch ring will be presented and compared in the result section.

2.3. Limit analysis formulation

Now we have obtained all the elements updated for the Upper bound (UB) limit analysis. The optimization problem can be formalized as Eq. (20a). We collect the new geometric compatibility condition (6) and flow rule for interfaces (10a) and elements (15a). Note that the external load must produce positive work on the structure, i.e. $\mathbf{f}_L^T\mathbf{u}>0$, and normalized form of this condition can be stated as $\mathbf{f}_L^T\mathbf{u}=1$ according to [27], known as the positive work condition. The in-element dissipation is also supplemented in the objective function. Here, $\mathbf{f}_D$ and $\mathbf{f}_L$ are vectors collecting all the dead and live loads applied to the blocks.

$$\begin{aligned}&\text{minimize} && -\mathbf{f}_D^T\mathbf{u}+\mathbf{c}_0^T\mathbf{p}+\mathbf{c}_1^T\boldsymbol{\lambda}\\ &\text{subject to} && \mathbf{f}_L^T\mathbf{u}=1\\ &&& \mathbf{A}_u^T\mathbf{u}+\mathbf{A}_\varepsilon^T\boldsymbol{\varepsilon}=\mathbf{q}\\ &&& \mathbf{N}^T\mathbf{p}=\mathbf{q},\ \mathbf{p}\geqslant\mathbf{0}\\ &&& \mathbf{M}^T\boldsymbol{\lambda}=\boldsymbol{\varepsilon},\ \boldsymbol{\lambda}\geqslant\mathbf{0}\end{aligned} \tag{20a}$$

$$\begin{aligned}&\text{minimize} && -\mathbf{f}_D^T\mathbf{u}+\mathbf{c}_0^T\mathbf{p}\\ &\text{subject to} && \mathbf{f}_L^T\mathbf{u}=1\\ &&& \mathbf{A}^T\mathbf{u}=\mathbf{q}\\ &&& \mathbf{N}^T\mathbf{p}=\mathbf{q},\ \mathbf{p}\geqslant\mathbf{0}\end{aligned} \tag{20b}$$

Removal of the terms that account for the deformability of the block elements will make the formulation degraded into the rigid block cases (Eq. (20b)) and the optimization formulation becomes the same as the one of classical rigid block limit analysis [25,28].

$$\begin{aligned}&\text{maximize} && \alpha\\ &\text{subject to} && \mathbf{A}_u\mathbf{x}=\alpha\mathbf{f}_L+\mathbf{f}_D\\ &&& \mathbf{A}_\varepsilon\mathbf{x}+\widetilde{\boldsymbol{\sigma}}=\mathbf{0}\\ &&& \mathbf{N}\mathbf{x}-\mathbf{z}_0=\mathbf{c}_0,\ \mathbf{z}_0\leqslant\mathbf{0}\\ &&& \mathbf{M}\widetilde{\boldsymbol{\sigma}}-\mathbf{z}_1=\mathbf{c}_1,\ \mathbf{z}_1\leqslant\mathbf{0}\end{aligned} \tag{21a}$$

$$\begin{aligned}&\text{maximize} && \alpha\\ &\text{subject to} && \mathbf{A}_u\mathbf{x}=\alpha\mathbf{f}_L+\mathbf{f}_D\\ &&& \mathbf{N}\mathbf{x}-\mathbf{z}_0=\mathbf{c}_0,\mathbf{z}_0\leqslant\mathbf{0}\end{aligned} \tag{21b}$$

The Lower Bound (LB) formulation (Eq. (21a)) can be obtained through writing the dual problem of Eq. (20a). Compared with the standard LB limit analysis for rigid block system (Eq. (21b)), we have to add a balance condition that associates the interfacial resultant **x** and in-element generalized force $\widetilde{\boldsymbol{\sigma}}$, as well as a constitutive condition to constrain these generalized force unknowns.

Finally, we observe the energy balance implied in the equilibrium and compatibility conditions. We pre-multiply the velocity **u** and strain rate vector **ε** by the equilibrium constraints in the LB formulation and sum them together (left side of Eq. (22)). The right-hand-side expression can be deduced by substituting the compatibility condition Eq. (6). Here, P_D^E and P_D^C are the internal power induced by interfacial and deformation-induced dissipation while the P_E and P_G are the external work done by dead and live loads. As a result, we see a balance of the internal dissipation and external works in each pair of static-equilibrium systems and compatible mechanisms.

$$\mathbf{u}^T\mathbf{A}_u\mathbf{x}+\boldsymbol{\varepsilon}^T\mathbf{A}_\varepsilon\mathbf{x}+\boldsymbol{\varepsilon}^T\widetilde{\boldsymbol{\sigma}}=\mathbf{u}^T\alpha\mathbf{f}_L+\mathbf{u}^T\mathbf{f}_D\Rightarrow\underbrace{\mathbf{q}^T\mathbf{x}}_{P_D^E}+\underbrace{\boldsymbol{\varepsilon}^T\widetilde{\boldsymbol{\sigma}}}_{P_D^C}=\underbrace{\mathbf{u}^T\alpha\mathbf{f}_L}_{P_E}+\underbrace{\mathbf{u}^T\mathbf{f}_D}_{P_G} \tag{22}$$

3. Benchmark case study

To gain deep insight into the properties of the proposed block element with different constitutive linearizations, we perform the collapse analysis of a circular arch ring with 80 blocks in this section as a benchmark study (Fig. 4). The geometric characteristics follow the ring of Prestwood Bridge, investigated in [13,14]. The span of the bridge is 6550 mm, with a rise of 1428 mm. The thickness of the arch ring is 220 mm. The out-of-plane depth of the arch is 3800 mm. The external load is applied at approximately the quarter span of the arch.

Material characteristics of the bricks are set referring to [14] (Table 1). The collapse of the rigid arch ring will also be presented (solved by Eqs. (20b) and (21b)) as a comparison to further understand how deformability influences the ring behavior at the collapse. When investigating the collapse of the deformable ring, as mentioned above, both quadrilateral- and hexagon-linearized constitutive (Eqs. (13) and (18)), will be taken into account.

3.1. Collapse of rigid and deformable arch ring

The collapse mechanism of the rigid arch ring is a standard 4-hinge

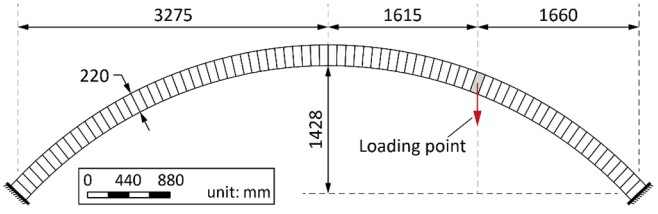

Fig. 4. Geometric features, loading and boundary conditions of the 80-block arch ring.

Table 1
Material feature of the bricks.

Density ρ_b [kg/m^3]	Interfacial cohesion c_{bb} [MPa]	Compressive strength σ_{bc} [MPa]	Tensile strength σ_{bt} [MPa]	Frictional angle φ_{bb} [°]
2000	10^{-6}	4.5	0	37

(S4H) mechanism (Fig. 5). Two extrados hinges are located at the loading point and left springer of the ring and two intrados ones are near the left quarter-span point and right springers. Such overall motion of the ring is commonly reported in the previous works (see [28–30,6,7]).

Adoption of the hexagon linearization could bring about the brick elements with insufficient consideration of the deformability. The predicted collapse mechanism of the ring remains unchanged: the ring remains a 4-hinge collapse (Fig. 6c and d), being no different from the rigid case as well as the same load prediction (Fig. 5). That makes sense given the expansion of the static-allowed area caused by the upper bound approximation. As we can read in Fig. 3b, the ultimate moment of the hexagon-linearized constitutive is twice the quadrilateral one in a low-compression condition, and the brick elements will thus perform a high resistance to the bending deformation. As a result, the dissipation of such element is more expensive than the appearance of the interfacial separations, resulting in the same ring collapse as the rigid modeling. The plot of the power dissipation further illustrates such consistency (compare these two cases in Fig. 7).

The collapse of the ring becomes different after applying the

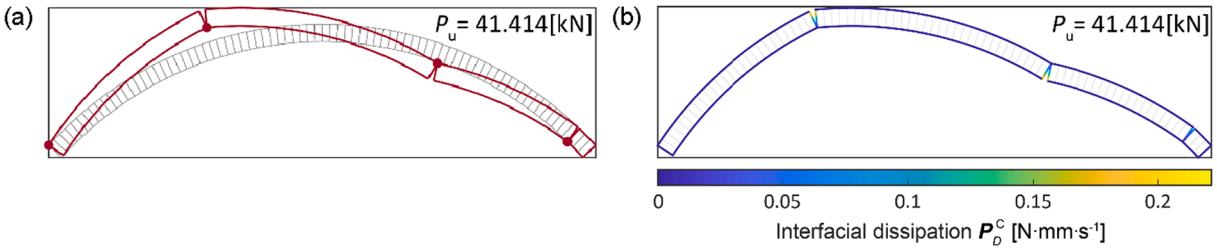

Fig. 5. Collapse of the rigid arch ring: (a) mechanism; (b) interfacial dissipation.

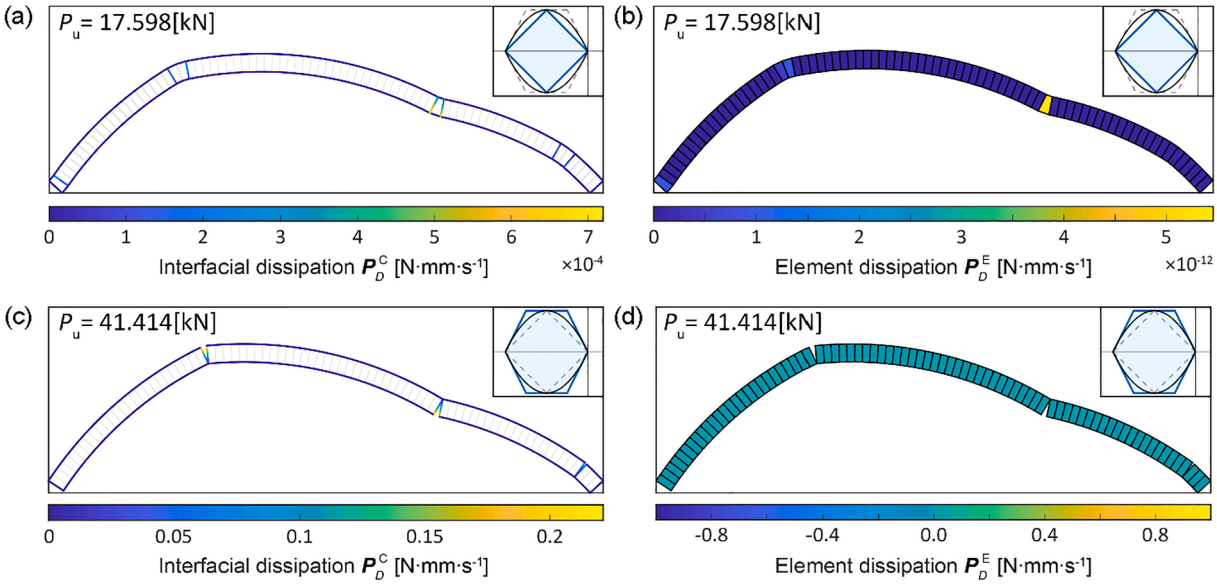

Fig. 6. Collapse of the deformable arch ring: (a) quadrilateral linearization, interfacial dissipation; (b) quadrilateral linearization, in-element dissipation; (c) hexagon linearization, interfacial dissipation; (d) hexagon linearization, in-element dissipation.

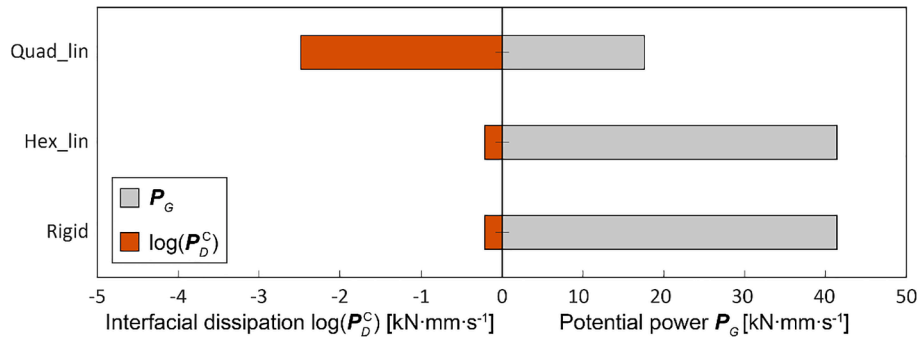

Fig. 7. Power dissipation in the collapse of the 80-block arch: comparison of rigid modeling, hexagon linearization, and quadrilateral linearization.

quadrilateral linearization. In this mechanism, all the interfacial separations, originally presented in the previous two S4H mechanisms, are shared by the bending deformation of the brick, and the magnitude of the overall motion is thus scaled down. The location of the deformed bricks agrees with the 4 hinges of the S4H motion (compare Fig. 6b and Fig. 5b) and these deformations present almost zero dissipation. Such moderate collapse deformation is manifested, in the aspect of power dissipation, as a lower potential power (see Fig. 7). Compared with the rest two cases, we can note the decline of the potential power has exceeded 50 %. Note that the load prediction in this benchmark case is dominantly contributed by the potential power (the magnitude of the dissipation is infinitesimal, around 10^{0}–10^{-3}, see Fig. 7). The reduction of the potential power will directly impact the capacity prediction. Therefore, the collapse load predicted from the quadrilateral linearization becomes discrepant from the other two rings, with a remarkable drop of 57.5 %. These results further demonstrate that the lower bound property of quadrilateral linearization gives the brick element better flexibility (in particular the deformation with zero dissipation), corresponding to the insertion of extra degrees of freedom in the structure. The displacement of the ring can thus be moderated when the collapse happens.

3.2. Parametric studies

Below we proceed to conduct several sensitivity analyses to better investigate the collapse performance of the ring under different material conditions. We start from the parametric study on the friction angle φ_{bb}, which ranges from 3° to 40°. As the curves illustrated (Fig. 8), hexagon linearization always gives a higher collapse load prediction because of its upper bound approximation. The sliding will appear at the interfaces when the friction condition degrades. If the friction angle drops below 14°, the collapse will transform from the S4H motion to the one mixed with hinges and sliding (HS). Sliding-hinge-mixed failure appears at the loading point and the hinge originally presented at the left springers is replaced by pure sliding. Further reduction of the friction (below 4°) will make the ring present a three-part collapse, purely with sliding failure at the interfaces (PS). Note that when using the hexagon linearization, all the block elements in the ring are not deformed in the investigated range of the friction angle, and this will also reason from the upper bound property of the hexagon linearization, which makes the brick element more resistant to the bending failure.

However, regarding the ring adopting the quadrilateral-linearized constitutive, the resistance of the brick elements is relatively low: we note several bricks deform with remarkable bending motion. Two collapse mechanisms with sliding are observed at a low friction level as well. TS1 mechanism presents a similar deformed configuration to the HS mechanism. Only the hinges in the HS mechanism are substituted with the bending bricks with zero dissipation. When the friction angle reduces below 3°, the location of the right failed brick in the mechanism (TS2) will be closer to the keystone and the collapse load further decreases. The decrease of the collapse load is almost linearly associated with the friction angle after the appearance of the sliding, no matter which linearization is employed. In the case of extremely low friction, the difference in load prediction from quadrilateral and hexagon linearization will be narrowed.

Then, the collapse performance of the arch with different compressive strengths of the brick (or macro block of masonry) is investigated. In this parametric study, the friction angle φ_{bb} is fixed at 37°, with a variation of the compressive strength σ_{bc} from 0.14 to 1 MPa. We keep holding the assumption of NTR material for the bricks, i.e. the tensile strength σ_{bt} is always zero. The results are illustrated in Fig. 9.

Again, we see a greater load prediction when employing the hexagon-linearized NTR constitutive. Thanks to the high resistance to bending failure, in all the collapse mechanisms that we find, only crushing of the block takes place. When the strength drops to a moderate level (0.45–0.6 MPa), the brick at two springers begins to fail due to compression. Two hinges at the middle of the arch remain unchanged (2C2H). Corresponding to this crushing-hinge-mixed mechanism, the evolution of the collapse load is nonlinear. After the strength drops below 0.45 MPa, no hinge appears in the mechanism anymore, instead by the crushing-induced failures of the bricks (4C1). The most severe crushing happens at the bricks near the loading point. At this stage, the capacity of the ring becomes linearly influenced by the compressive strength of the brick, as the dissipation power now almost stems from the compressing failure of the bricks. Once we employ the quadrilateral-linearized constitutive, bending failure of the bricks (see blocks with red frame highlighted in Fig. 9) will take place instead of the separations at the interfaces. Regarding this modeling, it seems that the capacity of the ring is less sensitive to the brick strength since the range of the brick strength corresponding to the stable stage of the curve is quite broad. This could arise from the presence of those bending bricks, which reduces the collapse motion of the arch, and the compressive stress at the springers could thus decrease. When we notice the first appearance of the crushing in the mechanism, the compressive strength of the brick has degraded to a deficient level (<0.26 MPa). When the capacity of the brick further decreases (<0.2 MPa), crushing will also be presented at

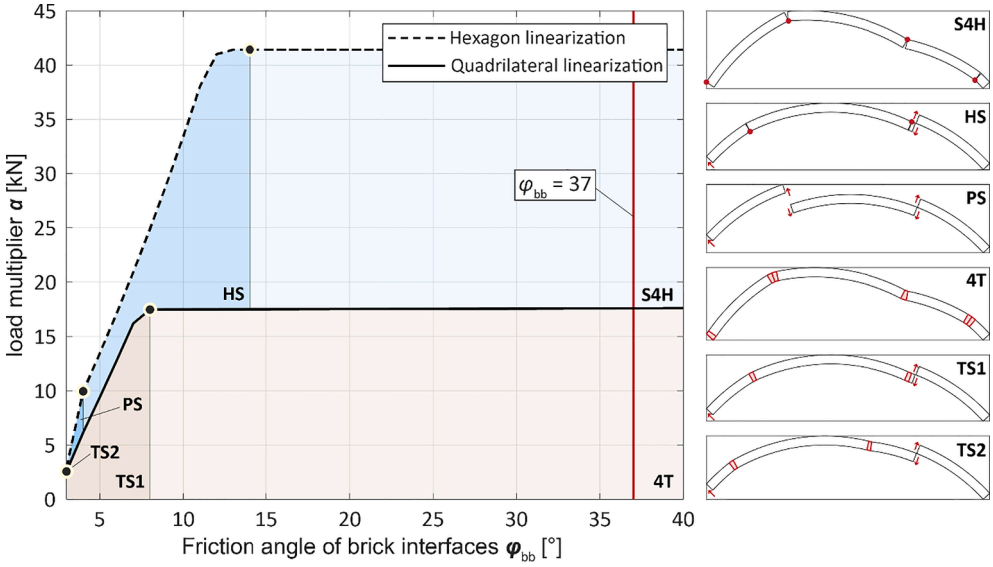

Fig. 8. Sensitivity analysis on friction angle of brick interfaces φ_{bb}: comparison of quadrilateral and hexagon linearizations, σ_{bc} = 4.5 MPa, σ_{bt} = 0 MPa.

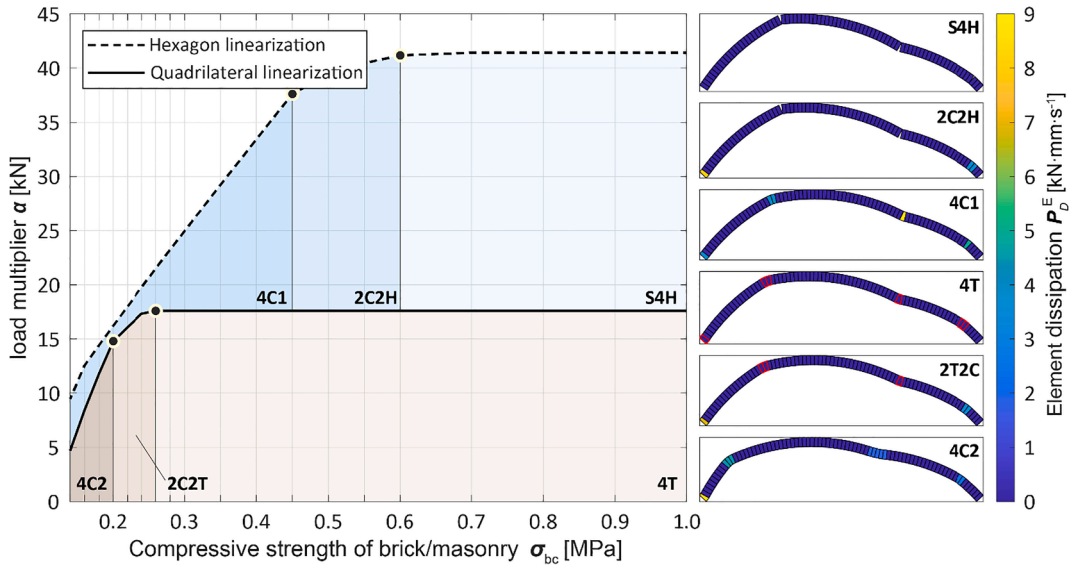

Fig. 9. Sensitivity analysis on compressive strength of the brick/masonry σ_{bc}: comparison of quadrilateral and hexagon linearizations, $\varphi_{bb} = 37°$, $\sigma_{bt} = 0$ MPa.

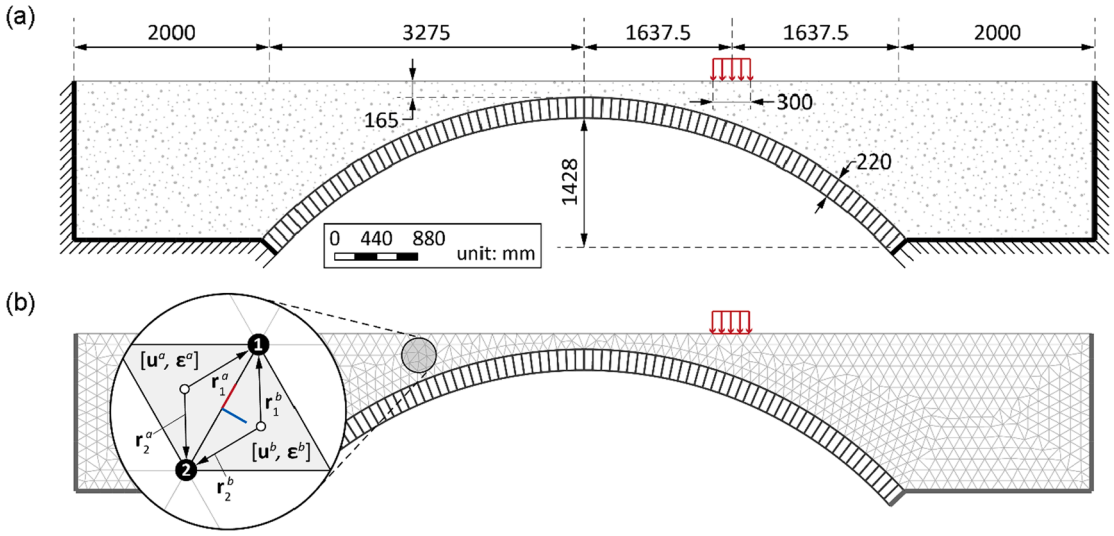

Fig. 10. Modeling of Prestwood Bridge: (a) geometric characteristic; (b) backfill modeling, external load and boundary conditions.

the middle of the arch and the drop in the load capacity of the arch is accelerated. In addition, the load prediction from two linearized constitutive models will get close when the compressive strength of the brick is low.

4. Application to masonry arch bridge with full consideration of backfill

In this section, we apply the proposed elements to analyze the collapse of the entire Prestwood Bridge with full consideration of the backfill, to investigate the robustness of such modeling in a more practical and large-scale scenario. The thickness of the fill at the top of the ring is 165 mm and the width of the wings on two sides is 2000 mm (Fig. 10a). The considered load pattern is also a quarter-span loading acting on the super surface of the fill. The width of the pressure is 300 mm. The boundary conditions at the side and bottom of the backfill as well as the springer are all unilateral contacts (Fig. 10b).

The backfill region is discretized by constant-strain triangular elements (Fig. 10b, left circle), proposed in the work from Sloan and Kleeman [23] (also being followed in the contributions of Cavicchi and Gambarotta [13,14]). Below we first elaborate on the integration of this element into the theoretical framework proposed in Section 2. Eq. (23) defines the space for the constant-strain mode $\mathscr{C}$. The induced velocity field can be generated from the strain components through the same standard form (Eq. (24)). Thus, using $\mathbf{H}^i_{\mathscr{C}}(\mathbf{r}^i)$ to update the deformation space mapping $\mathbf{H}^i_{\mathscr{S}}(\mathbf{r}^i)$ in Eq. (5b), we can soon get the new compatibility condition for the homogenous-deformed element, and this constraint shares the same matrix form as the proposed brick element (see Eq. (6)).

$$\mathscr{C}(E_i) := \left\{\mathbf{B}_S \cdot \mathbf{r}^i : \mathbf{B}_S \in \mathbb{R}^{2\times 2}, \mathbf{B}_S^T = \mathbf{B}_S\right\} \tag{23}$$

$$\mathbf{u}^i_{\mathscr{C}}(\mathbf{r}^i) = \begin{bmatrix} x-\bar{x}^i & 0 & y-\bar{y}^i \\ 0 & y-\bar{y}^i & x-\bar{x}^i \end{bmatrix} \begin{bmatrix} \varepsilon^i_x \\ \varepsilon^i_y \\ \varepsilon^i_{xy} \end{bmatrix} = \mathbf{H}^i_{\mathscr{C}}(\mathbf{r}^i)\boldsymbol{\varepsilon}^i \tag{24}$$

Regarding the constitutive model, we employ the standard Mohr-Coulomb yield criterion (25a) [31] with tension cut-off (25b) to describe the behavior of the fill elements, following the modeling in

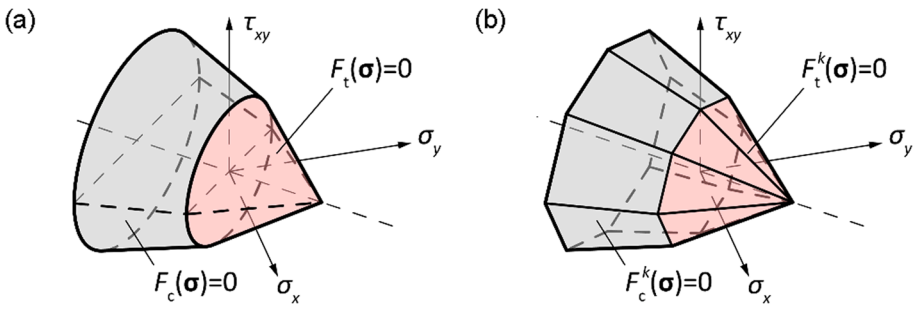

Fig. 11. Limit surface of 2D Mohr-Coulomb friction model with tension cut-off: (a) original limit surface; (b) linearizing approximation of the real surface.

[14]. Due to the nonlinearity of Mohr-Coulomb criterion and tension cut-off (Fig. 11a), we again adopt the linearization technique to approximate the real limit surfaces (Fig. 11b) [32], and then the associated flow rule can be stated as a linear constraint. The linearizations of these two criteria have very similar expressions (Eq. (26a)). We use in total p planes to linearize each criterion and A^k, B^k and C^k are the coefficients to represent the kth plane. The subscript "c" or "t" indicates linearization coefficients for the Mohr-Coulomb or tension cut-off model (Eq. (26b)). In this study, the precision of the linearization p for the backfill is set as 24 referring to [14]. All these constitutive constraints, flow rule, and dissipation terms can be expressed as the same linear matrix form to Eqs. (14a), (15a) and (16). Interfacial flow among the backfill elements and bricks uses the same associated Mohr-Coulomb flow rule (see Eqs. (8a), (10a) and (11)). Therefore, we can keep employing the same equations (Eqs. (20a) and (21a)) to solve the collapse of the bridge after the consideration of the fill.

$$F_c(\sigma_x,\sigma_y,\tau_{xy}) = (\sigma_x-\sigma_y)^2+(2\tau_{xy})^2-(2c\cos\varphi-(\sigma_x+\sigma_y)\sin\varphi)^2=0 \tag{25a}$$

$$F_t(\sigma_x,\sigma_y,\tau_{xy}) = (\sigma_x-\sigma_y)^2+(2\tau_{xy})^2-(2\sigma_t-(\sigma_x+\sigma_y))^2=0 \tag{25b}$$

$$\begin{aligned} F_c^k(\sigma_x,\sigma_y,\tau_{xy}) &= A_c^k\sigma_x+B_c^k\sigma_y+C_c^k\tau_{xy}-2c\cos\varphi=0 \\ F_t^k(\sigma_x,\sigma_y,\tau_{xy}) &= A_t^k\sigma_x+B_t^k\sigma_y+C_t^k\tau_{xy}-2\sigma_t=0 \end{aligned} \tag{26a}$$

$$\begin{cases} A_c^k=\sin\varphi+\cos a_k \\ B_c^k=\sin\varphi-\cos a_k \\ C_c^k=2\sin a_k \end{cases}, \begin{cases} A_t^k=1+\cos a_k \\ B_t^k=1-\cos a_k \\ C_t^k=2\sin a_k \end{cases}, a_k=2\pi k/p, k=1,2,\ldots,p \tag{26b}$$

Triangular mesh for the backfill region is generated through a MATLAB-based package "MESH2D" [33]. The typical size of the element is about 131 mm. The total amount of the element for backfill is 1605. Material parameters for the brick, backfill, and interfaces are given in Table 2. We use the same properties for the brick and its interfaces as the ones in the previous section. Parameters of the fill and its interfaces refer to [14]. The cohesion for the brick-to-backfill interfaces is also basically ignored. Similarly, below we will present the collapse of the bridge with the rigid or deformable ring, also investigating the effect of using different linearized constitutive model in the scenario involving ring-fill interaction.

Table 2
Material parameters for the brick, backfill and interfaces.

Elements		
Brick	Density ρ_b [kg/m^3]	2000
	Compressive strength σ_{bc} [MPa]	4.5
	Tensile strength σ_{bt} [MPa]	0
Backfill	Density ρ_f [kg/m^3]	2000
	Frictional angle φ_f [°]	37
	Cohesion c_f [MPa]	0.01
	Tensile strength σ_{ft} [MPa]	0
Interfaces		
Frictional angle	Brick to brick φ_{bb} [°]	37
	Brick to backfill φ_{bf} [°]	37
	Backfill to backfill φ_{ff} [°]	37
Cohesion	Brick to brick c_{bb} [MPa]	10^{-6}
	Brick to backfill c_{bf} [MPa]	10^{-6}
	Backfill to backfill c_{ff} [MPa]	0.01

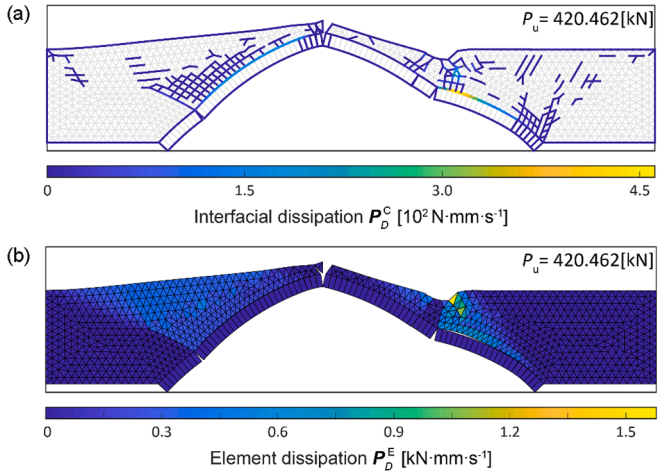

Fig. 12. Collapse of Prestwood Bridge, rigid arch ring: (a) interfacial dissipation; (b) in-element dissipation.

4.1. Collapse of the bridge with different modeling of the arch ring

We first investigate the collapse of the bridge with the rigid ring (Fig. 12). After considering the backfill, the overall motion of the rigid ring is basically consistent with the S4H mechanism (see Fig. 5) while the number of hinges significantly increases. Clusters of intrados hinges occur near the keystone and right springer. The location of the presenting hinges agrees with the one indicated in S4H. Regarding the motion of the backfill, the external loaded area moves downward, and the left side rises due to the passive extrusion from the ring. Below the external surface loading, there is a trapezoid region of backfill elements that presents a large strain rate. Note that the distance between the extrados hinges is larger than the origin width of the surface pressure. This indicates that the load has been dispersed by the backfill before it is transferred onto the arch ring. Meanwhile, the left passive-extruded backfill experiences large deformation as well, with a distribution of high dissipation energy. The crack propagation in the backfill follows the region of large dissipation. We also notice some short cracks spreading at the backfill above the right springer, which could be attributed to the occurrence of the separation at the extrados of the right springer.

Involving the ring deformability generally does not influence the overall collapse motion of the bridge. When applying the hexagon-linearized constitutive, we only note that the keystone brick deforms

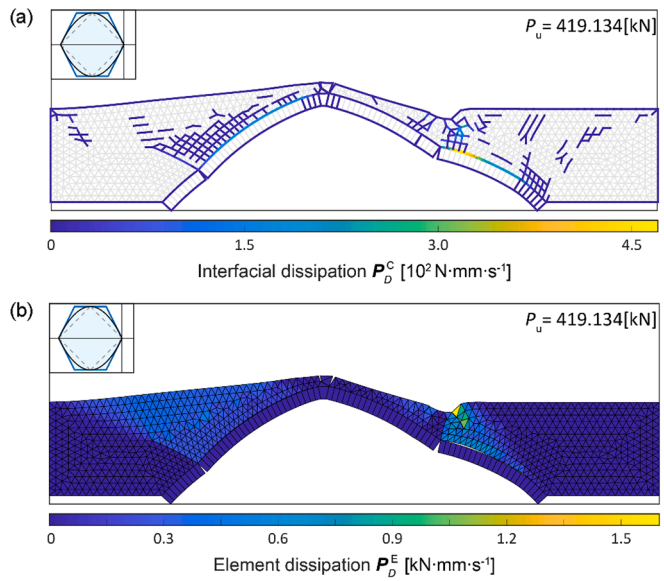

Fig. 13. Collapse of Prestwood Bridge, deformable arch ring, hexagon-linearized constitutive: (a) interfacial dissipation; (b) in-element dissipation.

due to bending failure, and the locations of other hinges remain the same as the one presented in the rigid-arch case (Fig. 13). Thanks to the bending of the keystone, the deformation of the backfill upon the keystone becomes more continuous. However, those changes in the mechanism have a minor impact on the load capacity of the bridge, with a deviation of only 0.32 % compared to the case of rigid-ring modeling.

The adoption of quadrilateral linearization will significantly cut down the load prediction thanks to its lower-bound-approximated property. Compared to the case of the rigid arch, the drop of the load could reach 46.3 %, and this prediction exceptionally agrees with the experimental study [34] (with only a bias of 0.98 %). Regarding the mechanism, again we see a more flexible behavior of the brick elements when the collapse happens. All the interfacial discontinuities of the ring vanish, being shared by the deformation of the bricks (Fig. 14). Zero dissipation of these failed bricks indicates that those failures are caused by the occurrence of tensile stress on the section. Compared to the location of the left hinge in the previous two cases, we note that in this

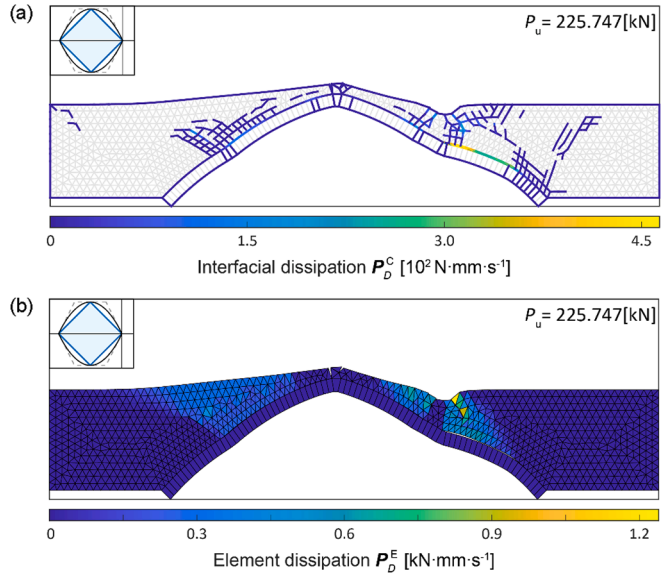

Fig. 14. Collapse of Prestwood Bridge, deformable arch ring, quadrilateral-linearized constitutive: (a) interfacial dissipation; (b) in-element dissipation.

case, two bending bricks at the left side get closer to the keystone, and the passive motion of the ring in the predicted mechanism is moderated. As a consequence, both the passive-extruded area and the crack propagation at the left part of the backfill are shrunk. The cracks at the right springers also become fewer.

These aspects can be quantitatively demonstrated again through the power proportion chart of the bridge collapse (Fig. 15). Given that negligible dissipation appears in the brick elements and at their interfaces, only the dissipation power of the fill is plotted here. We also distinguish the potential power of brick or backfill elements (subscripts "f" or "b" in Fig. 15 denote brick or backfill, respectively). Note that in the collapse that involves the ring-fill interaction, the power dissipation in the backfill gains a considerable proportion, and a more flexible ring modeling (quadrilateral linearization) will give rise to a remarkable decline in this part of dissipation, resulting in a more conservative collapse load prediction. The decrease in plasticity dissipation of backfill is caused by, as we have mentioned, the reduction of the passive-extruded backfill, among which the decrease of element dissipation is more prominent (about 34.3 % compared to the case of hexagon linearization). Besides, the degradation of the potential power in the backfill is even more noticeable, which can reach 59.7 %. This should also be a consequence of the shrinkage of the passive-extruded backfill since it will contribute to the alleviation of the backfill motion at the left. Therefore, we can conclude that the different modeling of arch flexibility majorly impacts the prediction of the passive-extrusion area in the backfill. Benefiting from the flexible ring modeling, both dissipation and potential power that take place in this area will be prominently lower, and load prediction thus becomes conservative.

4.2. *Parametric studies*

Below we conduct the sensitivity analysis on the compressive strength of the brick (or macro block of masonry) to further understand how the deformability of the ring affects the load capacity of the bridge. All the setting of the material features follows the previous analysis. We vary the brick strength σ_{bc} from 0.5 to 8 MPa and the tensile strength of the brick σ_{bt} is again neglected, keeping the assumption of no-tensile resistance (NTR) for brick material.

The predicted curves for the two considered constitutive models demonstrate very analogous characteristics (Fig. 16) presenting also very similar trend to the curves in the previous pure arch investigation (see Fig. 9). When the compressive strength is high, the collapse load remains stable, and then it decreases associated with the fall of σ_{bc}. At the beginning, the drop of the load present non-linearity, indicating that the collapse mechanism of the bridge may transit. If the brick is vulnerable enough, the decline of the load capacity becomes linear. When employing hexagon linearization, the non-linear stage will begin at 3.5 MPa and the linear-drop stage follows when σ_{bc} is below 2 MPa. However, those strengths are still quite high for the case using quadrilateral linearization, where the load capacity of the bridge remains at the constant stage. The following non-linear stage is very narrow in this case and the drop of the collapse load soon reaches the linear stage ($\sigma_{bc} < 1$ MPa). At the constant-load stage, the load prediction given by the hexagon linearization gets very close to the result of the rigid arch modeling whereas the overestimation compared with the prediction of quadrilateral linearization, as well as the experiment result, becomes significant. Oppositely, when the σ_{bc} is small, the load prediction from the two different linearizations will become close (difference within 10 %).

We also give the collapse motion of several representatives (green squares denoted on the curves in Fig. 16), to demonstrate the transition of mechanism when the compressive limit of the bricks falls. Taking the results of the quadrilateral linearization as an example (left column of Fig. 17), along with the decline of the brick strength, we can observe an increasing occurrence of crushing failure at the bricks. The location of the crushing bricks is basically in line with the hinges in the S4H

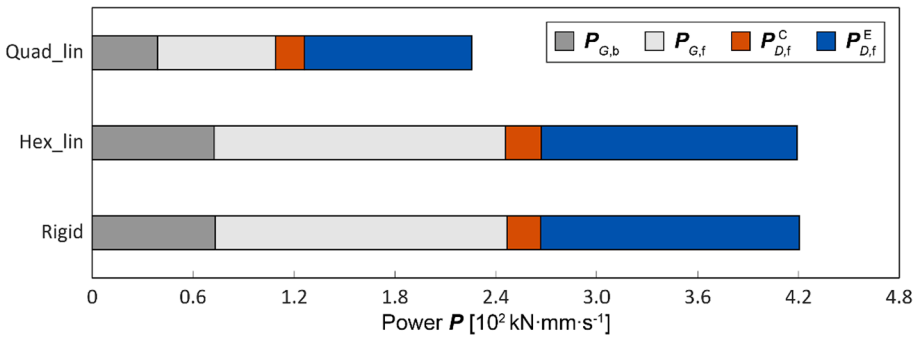

Fig. 15. Power dissipation in the collapse of Prestwood Bridge: comparison of rigid modeling, hexagon linearization, and quadrilateral linearization.

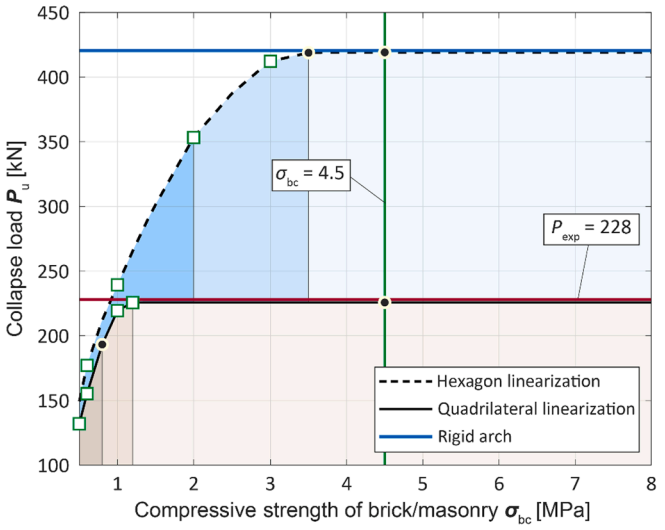

Fig. 16. Collapse load of the bridge P_u vs. compressive strength of brick/masonry σ_{bc}: comparison of deformable and rigid arch.

mechanism. The bricks at the right springer firstly crush due to the presence of high compressive stress (Fig. 17a). Then, at the non-linear drop stage, the severe deformation with a combination of axial compression and bending takes place at the keystone brick, presenting a remarkably high dissipation (Fig. 17c). After entering the linear drop stage, additional crushing happens at two bending blocks below the surface loading (Fig. 17e). When σ_{bc} drops to an extremely low condition, the two deformed bricks at the left span can also present compressive failure to some extent (Fig. 17g). The presence of those crushing bricks reduces the overall motion of the ring, and the dissipation in the backfill caused by the passive extrusion drops. Such conversion of the collapse mechanism for the case that adopts hexagon-linearized constitutive is analogous (right column of Fig. 17) while the predicted collapse load corresponding to a similar deformed configuration is higher.

On the other hand, to investigate the influence of backfill properties on the collapse behavior of the bridge, we then implement parametric studies on the cohesion and friction angle of backfill. Again, other material features are the same as in the previous analysis, and both rigid and deformable modeling, with different linearizations, for the ring are considered. The compressive strength of the brick σ_{bc} returns to 4.5 MPa. Corresponding interfacial parameters of the backfill vary along with the element ones (i.e. we keep $c_{ff} = c_f$, $\varphi_{ff} = \varphi_f$).

Fig. 18 gives the sensitivity curves of the collapse load regarding backfill cohesion c_f. The load curve for the case of adopting quadrilateral linearization exhibits a linear variation, which implies no change in the collapse mechanism. Regarding the rest two modelings for the arch, the trend of the sensitivity curves is bilinear. The slope of these two curves slightly decreases when the backfill cohesion is large. The collapse load predicted in these two cases is always overestimated compared with the result from quadrilateral linearization. The maximum overestimation could reach 56 %. The consistency of employing the rigid modeling and the deformable modeling with hexagon linearization only holds when the backfill cohesion is low ($c_f < 0.01$ MPa) whereas they will deviate along with the growth of the cohesion. When applying the backfill with high cohesion, the load predictions given by the three considered modeling of the ring can be quite different. That is to say, the predicted load will become more sensitive to different modelings of the arch in this case.

The influence of the friction angle of the backfill on the load capacity of the bridge is then investigated (Fig. 19). In the considered range of the backfill friction, the collapse load for all three bridges monotonically increases along the growth of the friction angle, with some slight non-linearity. Such a trend demonstrates that no distinct change in the collapse mechanism takes place. Again, we see a conservative prediction of the collapse load when employing the quadrilateral-linearized constitutive for the arch ring, and the rest two modelings give almost the same solution. A very small bias can be recognized when the friction angle is large. On these two curves, we note a significant turning point at $\varphi_f = 22°$, below which the drop of the collapse load will accelerate. In addition, compared with the backfill cohesion, the capacity of the bridge is less sensitive to the backfill friction.

Finally, we observe the effect of the material features of the backfill on the collapse motion of the bridge. The left column of Fig. 20 gives the collapse mechanism of the bridge applying a high-cohesion backfill ($c_f = 0.08$ MPa). In the case of quadrilateral linearization, the overall motion of the bridge agrees with the case under low cohesion, with a slight shrinkage of the left dissipation area (see Figs. 20a and 14b). However, we note a conversion of the collapse mechanism in the case of rigid arch after the increase of backfill cohesion. Comparing Fig. 20e with Fig. 12b, the passive-extrusion area of the backfill at the left significantly reduces, with also a remarkable drop of dissipation in this area. The possible reason could be that the large backfill cohesion will lead to worse deformability of the backfill and the containment stress that restrains the motion of the ring increases, which precludes the passive motion of the arch. Moreover, such large containment stress leads to the occurrence of sliding near the keystone. The presence of these slidings also moderates the deformation of the ring. Regarding the case of hexagon linearization, the effect of such large containment stress is manifested as the crushing failure of the brick that takes place at the keystone and springer (see Figs. 20c and 13b). This explains why the load prediction from the hexagon linearization deviates from the rigid modeling when the backfill cohesion is large.

The right column of Fig. 20 gives the collapse of the bridge with a low-friction fill ($\varphi_f = 22°$). Again, regarding the case that uses quadrilateral-linearized constitutive, the mechanism of the bridge is not influenced by the decrease of the backfill friction (see Figs. 20b and 14b). In contrast, in the other two cases, we see a severe local collapse of the backfill at the external loading area when applying the backfill with

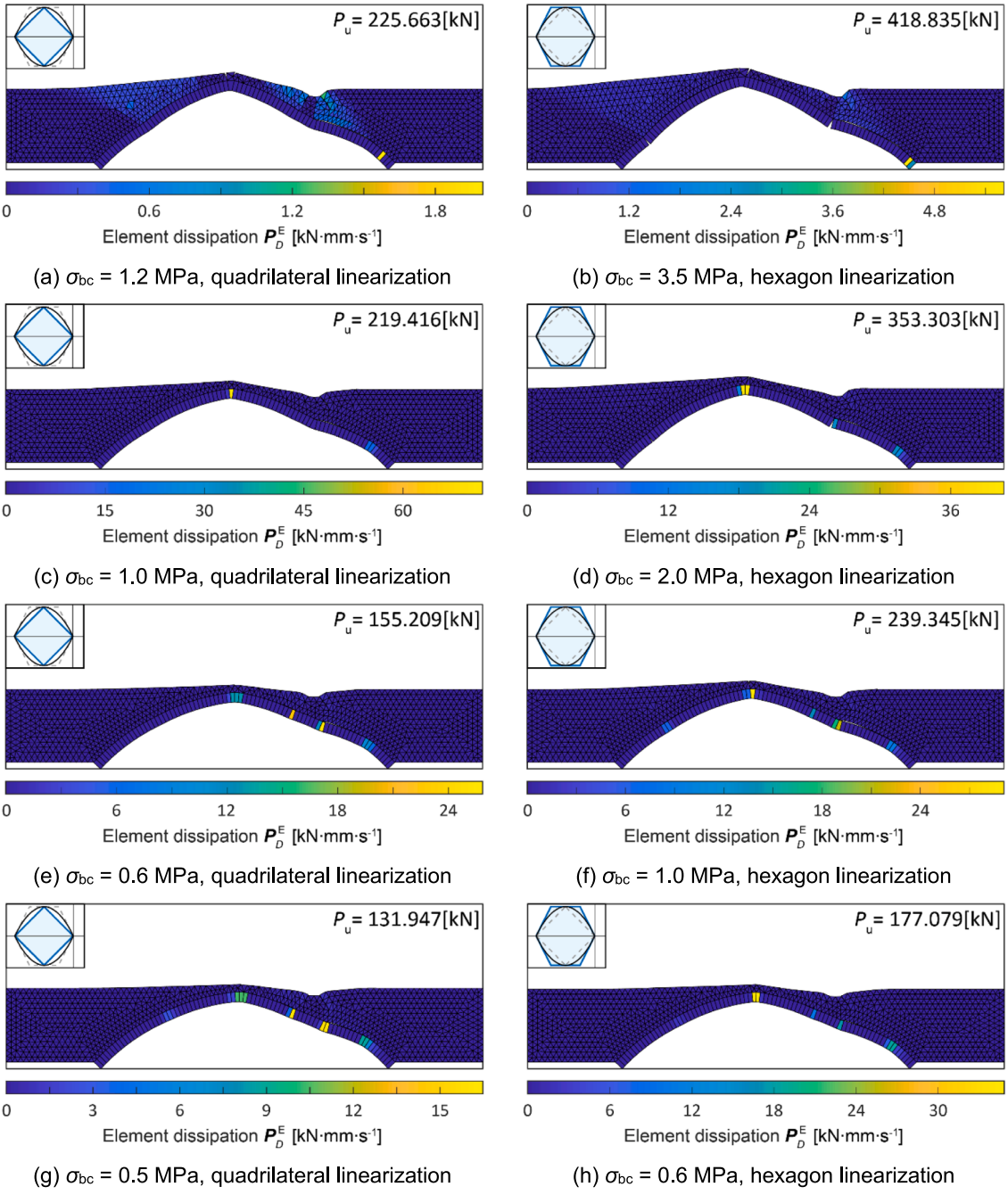

Fig. 17. Collapse mechanism of Prestwood Bridge under different brick strength conditions: in element dissipation.

weak friction while the deformation and dissipation of the left part of the backfill become inconsiderable (see Fig. 20d and f). As a result, when the fill friction degrades, the decline of the collapse load for these two cases speeds up and presents a completely linear trend associated with the drop of friction (Fig. 19).

5. Discussions

The collapse of Prestwood Bridge is an important benchmark study that has also been documented by pioneering researchers. As mentioned above, the contributions from Cavicchi and Gambarotta [13,14] are critical numerical works on this bridge, where thorough limit analysis investigations with full modeling of the backfill are carried out. Instead of using brick elements, they simplified the arch ring bricks into 80 beam elements, and the arch-fill interfaces are modeled through quadrilateral cohesion elements. Below discussion, we will first revisit some of their results and discuss the consistency and discrepancy compared with our predictions.

Before that, we would like to reproduce the collapse of the 80-block arch through the beam element modeling proposed by Cavicchi and Gambarotta [14], as a verification. This element consists of two nodes with three freedom each and one mid node that allows only the axial displacement. Compared with the construction of the velocity field proposed in this paper, these variables can further represent the space of axial deformation mode with high order in that the left and right half of the beam can have different axial strain and curvature. However, in their modeling, no velocity discontinuities were considered between the two beam elements. All the dissipation is reduced into two plastic hinges near the end nodes (Fig. 21a), and as mentioned in Section 2, the constitutive model employed for these hinges is the hexagon

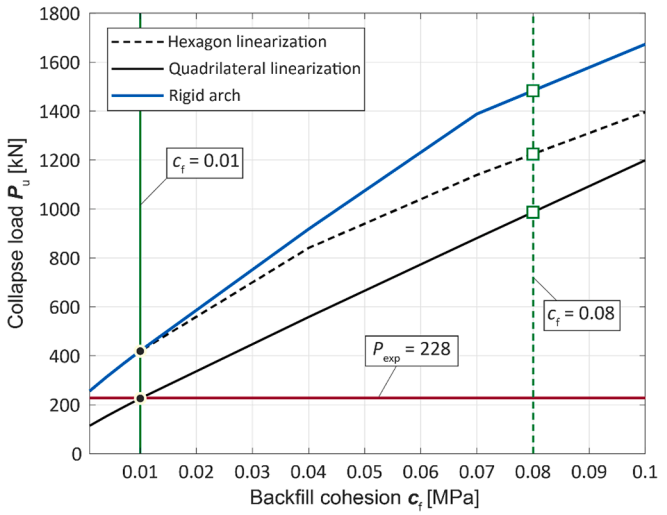

Fig. 18. Collapse load of the bridge P_u vs. backfill cohesion c_f: comparison of deformable and rigid arch.

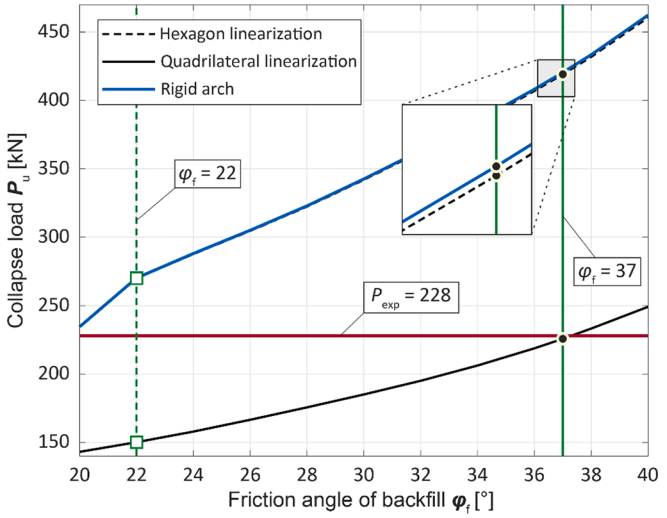

Fig. 19. Collapse load of the bridge P_u vs. friction angle of backfill φ_f: comparison of deformable and rigid arch.

linearization (Eq. (18)). Fig. 21b gives the collapse result of the arch ring through this beam element. Both overall motion and the location of the hinges predicted from the beam elements are in line with the collapse given by the brick elements (see our results of the hexagon linearization, Fig. 6c and d), with also a very comparable load prediction (bias within 1 %). This verifies the good accuracy of the proposed brick elements being applied to the collapse analysis of the pure arch case.

In Table 3, we also compare the computational efficiency of the brick elements and the beam element in the case of 80-block arch collapse. As we could expect, compared with the brick elements, usage of the beam element will lead to fewer constraints for the problem since the velocity jumps between the beams are ignored, while the optimization variables increase due to the assignment of more plastic hinges in each beam. Comparing the two deformable brick cases, the case of quadrilateral linearization has a comparably smaller problem size thanks to the adoption of fewer approximation planes in the linearization, and thus it comes up with lower time consumption (about 37.5 % lower than the case of hexagon linearization). The beam element performs an even faster prediction, whose time cost is about 47 – 73 % of the two deformable brick elements. However, we would still say the computational budget of the deformable brick element is acceptable given its extra consideration of the real geometry characteristics and interfacial discontinuities. These aspects were neglected in the beam elements.

We now proceed to compare our prediction of Prestwood Bridge to the simulation from Cavicchi and Gambarotta [14]. To make the results comparable, here we plot the distribution of the normalized plasticity multiplier over the bridge instead of the in-element dissipation (Fig. 22). We see that actually, the overall motion of the collapse is quite consistent, with the only discrepancy in the location of the left hinge. However, the location of this hinge is very critical to the final prediction as it defines the area of passive-extrusion backfill. As remarked in our results above, a large passive-extrusion area will significantly increase both plasticity dissipation and potential power in the backfill, leading to a high prediction of collapse load. When adopting the quadrilateral-linearized constitutive for the brick element, the location of the left hinge is the most adjacent to the keystone wherefore the area of the passive extrusion is the smallest (Fig. 22b). In contrast, this area predicted from the other two modelings is much more considerable (Fig. 22c and d), because of the remarkable passive motion of the arch. The passive-extrude area of the backfill given by the beam element modeling is between them (Fig. 22a). Note that, however, the predicted collapse load is significantly lower than the counterpart case that uses the deformable brick modeling with hexagon-linearized constitutive (Fig. 22c). Therefore, employing the beam element could give rise to over-deformable modeling of the ring in the collapse analysis that involves ring-fill interaction, which may arise from the simplified consideration of the arch geometry. The actual thickness of the arch is not explicitly taken into account in the analysis. Besides, the modeling of the cohesion element they proposed for the ring-fill interaction could be too conservative. Consequently, although Cavicchi and Gambarotta adopted a linearization with upper-bound property, the predicted load remains at a low level, matching the prediction from the brick element that uses the lower-bound-approximated (quadrilateral) linearization.

Another comparable numerical work could be the finite element analysis of Prestwood Bridge carried out by Drosopoulos et al. and Betti et al. [35,36]. In their analysis, the arch ring is discretized by 40 elastic blocks with interfaces modeled through unilateral frictional contact (Fig. 23). The backfill region is meshed by two-dimensional plane strain elements with Mohr-Coloumb plasticity. As illustrated in Fig. 23, we observe a considerable area of passive-extruded backfill, being very comparable to our prediction in the case where the ring lacks flexibility (i.e. the hexagon linearization or rigid ring cases, see Fig. 22c and d). Such overestimation of the passive motion may arise from the insufficient consideration of the discontinuities in the backfill region, resulting in more dissipation in the elements. However, the load prediction from the finite element analysis is more conservative than the limit analysis counterpart, which should be thanks to the usage of non-associated flow. In their modeling, the dilation angle of the backfill is smaller than the friction angle, giving rise to less pseudo-dilation in the fill region. This could imply the possible inaccuracy of assuming the associated flow for the backfill triangles. Overestimated element dilation could also lead to higher load prediction in limit analysis. Revisiting our predictions, the appliance of associativity for the joints should be acceptable since the interfacial dilation presented in the bridge collapse is quite limited. However, different assumptions of the element dilation mode may significantly affect the prediction of passive-participated fill, and this will further bias the load prediction. This sensitive factor will be highly considered in our future work.

Finally, we make a comparison to the previous experimental results. Prestwood Bridge is a real bridge that has been experimentally tested on-site. As reported by Page [34], the collapse load given from this on-site test is 228 kN (Fig. 24a). Compared with this experimental result, as mentioned above, the most accurate prediction from our numerical investigation is produced by the deformable brick element with the quadrilateral-linearized constitutive (225.747 kN), with a very compatible prediction of the collapse mechanism to the experiment results as well (Fig. 24b). In particular, the prediction of the location of the

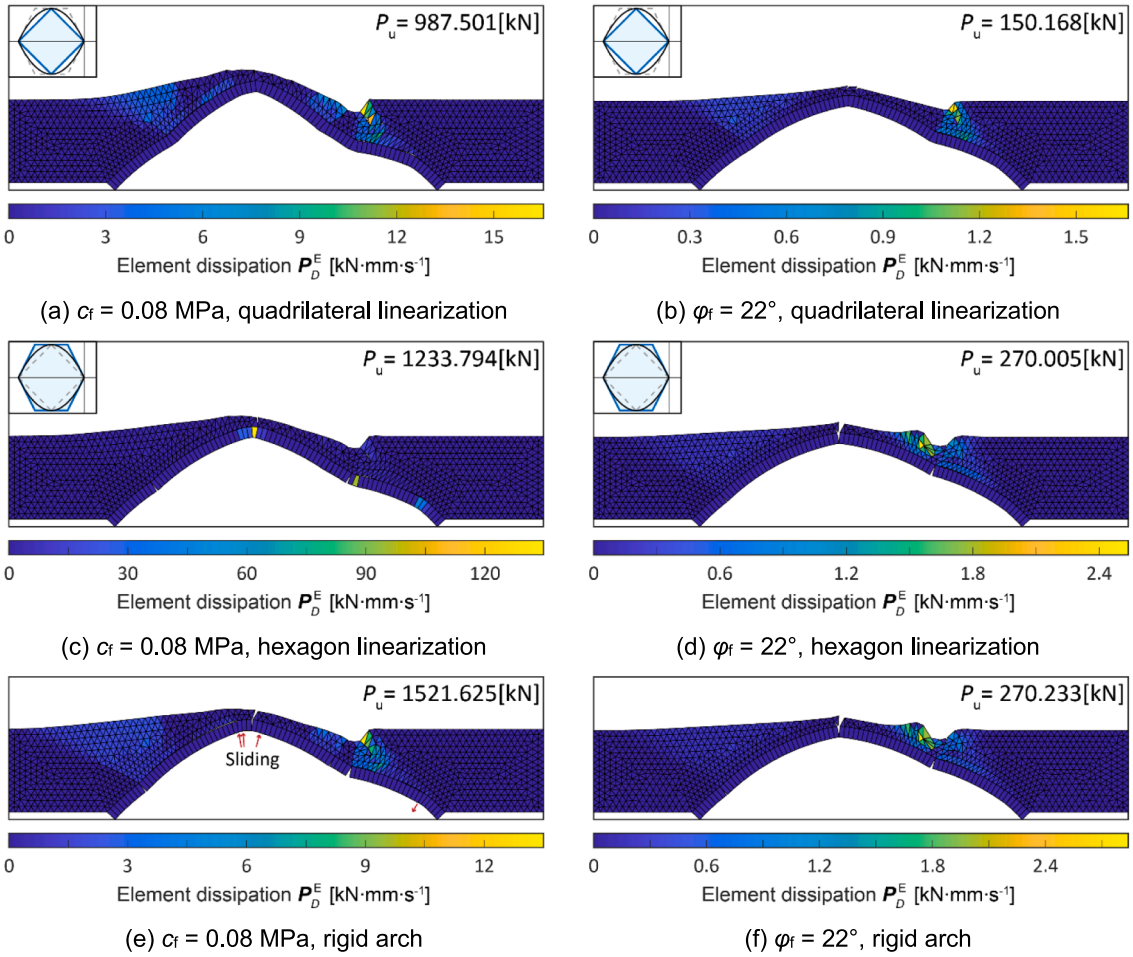

Fig. 20. Collapse mechanism of the bridge under different backfill cohesion and friction conditions: in element dissipation.

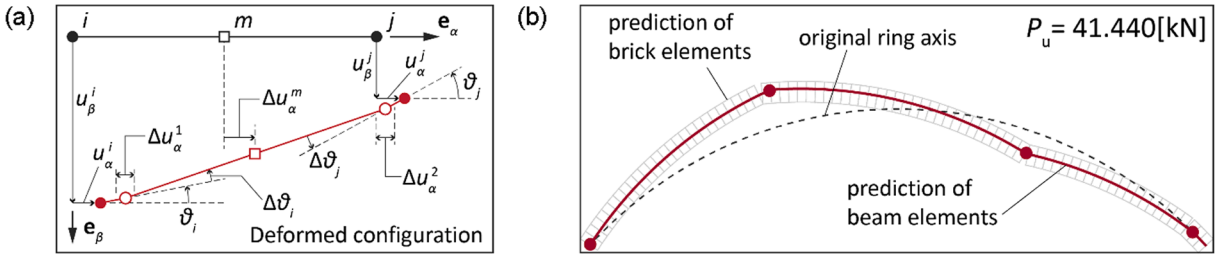

Fig. 21. Collapse of 80-block arch using the beam element proposed by Cavicchi and Gambarotta: (a) configuration of the beam element; (b) collapse results.

Table 3
Summary of collapse analysis on the 80-block arch case.

Element type	Element constitutive model	Load prediction [kN]	Problem size		Computational time [s]
			Constraints	Variables	
Deformable Beam	NTR, hexagon linearization	41.440	326	1283	0.02283
Rigid brick	–	41.414	324	564	0.02014
Deformable brick	NTR, hexagon linearization	41.414	484	1204	0.04797
Deformable brick	NTR, quadrilateral linearization	17.598	484	1044	0.03028

left hinge as well as the area of passive-extruded infill is in good agreement with the experimental mechanism, which is, as discussed above, very critical for a precise prediction of the load capacity. Regarding the other two considered cases, as we expected, the predicted area of the left passive-extruded backfill is noticeably larger than the experimental result. Furthermore, according to the parametric study of backfill properties (see Figs. 18 and 19), the predicted load of these two cases is still overestimated when the concerned parameters are reduced to an infinitesimal level. Although when the compressive strength is very low, the collapse load predicted in these two cases can be comparable to

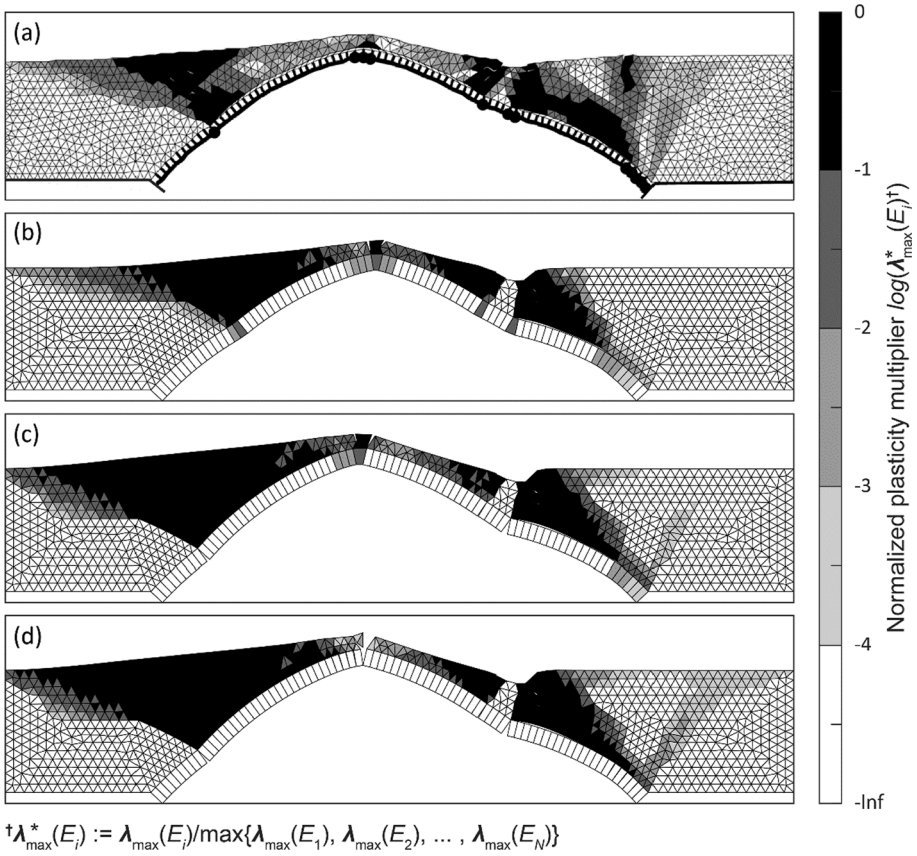

Fig. 22. Distribution of the normalized plasticity multiplier, collapse of Prestwood bridge, $c_f/c_{ff} = 0.01$ MPa, $\sigma_{bc} = 4.5$ MPa, $\varphi_f/\varphi_{ff}/\varphi_{bb} = 37°$: (a) prediction of Cavicchi and Gambarotta, $P_u = 228$ kN; (b) deformable arch ring, quadrilateral linearization, $P_u = 225.747$ kN; (c) deformable arch ring, hexagon linearization, $P_u = 419.134$ kN; (d) rigid arch ring, $P_u = 420.462$ kN.

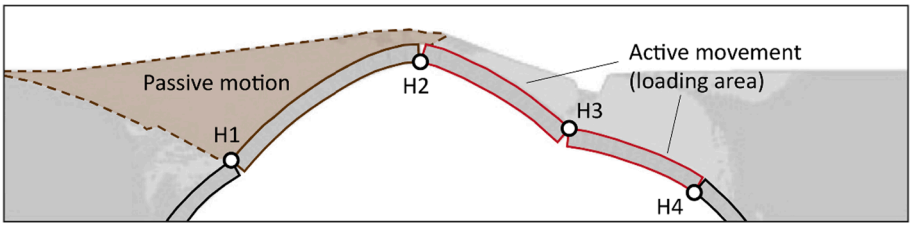

Fig. 23. Result of finite element analysis of Prestwood bridge carried out by Drosopoulos et al. and Betti et al.: 40-block ring, non-associated plasticity for the backfill, $P_u = 225.4$ kN.

the experiment result, the corresponding mechanism deviates (see Fig. 17f). Therefore, it can be concluded that the overestimation of the load prediction of these two modelings arises from the insufficient consideration of the ring flexibility, instead of the bias of the material properties.

We would point out at last that in the report from Page [34] no relevant material properties test on the stone or backfill is provided. The material parameters employed in our analysis are the calibrated values from the previous numerical works [13,14], and the accuracy of these material parameters could be debatable. Therefore, in the following works, we will apply the proposed element to other laboratory-tested benchmarks with available material properties. An in-scaled laboratory test of bridge collapse could also be expected in the future for the benchmark purpose.

6. Conclusions

In this paper, we have put forward a new limit analysis modeling for the arch ring in masonry arch bridges considering the deformability of the bricks. The velocity field of the proposed deformable brick element accounts for both the rigid body mode and the axial deformation mode induced by axial compression and bending deformation. No-tension resistance (NTR) constitutive relation has been applied to describe the material characteristic of the brick. Two different linearizations for this relation have been employed to preclude the nonlinearity in the constraints. As a consequence, the updated heterogenous limit analysis formulization with the inclusion of the deformable bricks remains a Linear Programming (LP) problem. Employing the proposed elements, we have performed the collapse analyses of an 80-block arch and the real Prestwood Bridge that involves the arch-ring interaction. Exhausted parametric studies on brick and backfill material properties have then been conducted. Finally, we have compared our predictions to the previous experimental and numerical pioneering contributions, discussing the influence of using different modelings of ring flexibility.

We have first investigated the properties of the proposed brick elements and different constitutive linearizations through the benchmark

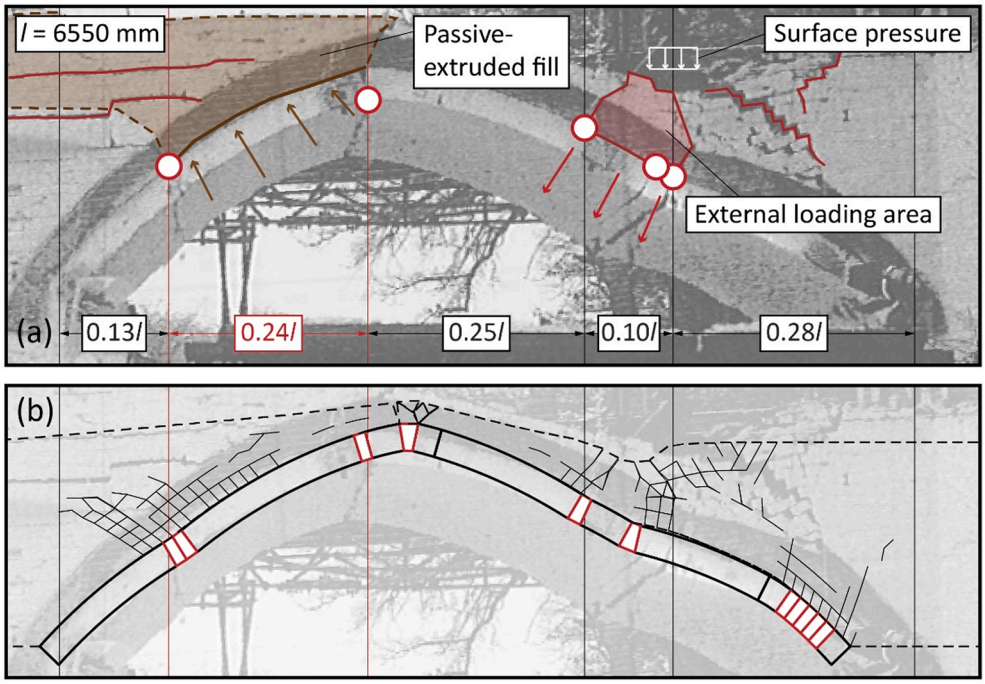

Fig. 24. Collapse mechanism of Prestwood Bridge from the on-site collapse test, reported by Page: (a) diagram of the test results, $P_{exp} = 228$ kN; (b) comparison with the prediction from the deformable brick element, quadrilateral linearization, $P_u = 225.747$ kN.

study of the 80-block arch. The element with hexagon-linearized constitutive performs comparably stiffer, whose behavior can be very close to the rigid block elements in the pure-arch case. In contrast, the quadrilateral linearization gives rise to a conservative load prediction due to its lower bound property. Such linearization will make the brick elements more vulnerable to tensile failure. Therefore, under a low axial compression condition, bending of the brick is more likely to take place. These bending deformations share separation at the interfaces, causing a moderate collapse motion of the ring. Crushing happens only when the compressive strength of the brick is extremely low (<0.6 MPa). In addition, the reproduced collapse analysis of this 80-block arch through the beam element (put forward by Cavicchi and Gambarotta [14]) also gives a compatible prediction to our results.

Collapse analysis on Prestwood bridge has further demonstrated that the proposed deformable brick elements can perform with good accuracy when applied to a practical and large-scale collapse analysis. When employing quadrilateral-linearized constitutive, the predicted collapse load is exceptionally close to the previous experimental result tested in-situ (with a deviation of 0.98 %). However, the hexagon linearization will give rise to an overestimated load prediction (discrepancy reaches 46.3 %), being again very comparable to the prediction of rigid modeling. This demonstrates that the modeling of the ring deformability is even more essential when analyzing the arch-fill interaction. Different modeling of the ring majorly influences the prediction of the passive extrusion of the fill. As indicated in the previous 80-block arch case, bricks with weak deformability will give rise to significant overall deformation of the ring, and in the collapse that involves arch-fill interaction, such large ring deformation will further enlarge the passive-extruded area of the backfill. The predicted load will thus increase since more dissipation, as well as potential power, is present in the backfill.

In conclusion, when investigating the arch-fill interaction of masonry arch bridges, the brick element with quadrilateral linearization is a recommended solution, considering its compatible prediction of both load and collapse mechanism to the experimental result. Nevertheless, given that the results predicted from the hexagon linearization are also in good agreement with the one from the reproduced beam element in the case of the 80-block arch, such upper-bound linearization may be accurate in the collapse analysis of some pure-arch cases. In addition, we would remark that the beam elements give rise to significantly conservative load prediction for Prestwood Bridge compared with the brick modeling when using the same hexagon linearization. This indicates that when analyzing the arch-fill interactions, employing beam elements for the ring modeling may present lower flexible resistance, which could be attributed to the neglect of the thickness of the ring. Although such modeling for the case of Prestwood Bridge can predict a precise collapse load, deviation may appear when applied to other practical cases due to such simplification. The deformable brick element proposed in this paper can be regarded as a theoretical generalization of the beam element, where both the real geometric characteristics and interfacial discontinuities between the blocks are taken into account. If the constitutive model for the element is properly considered, it can also be used as a macro-block modeling for the masonry material. Therefore, the proposed brick element can provide the community with a more general alternative to modeling the arch or vault structures in limit analysis.

Future work will implement this modeling to analyze the collapse of other benchmark examples to further test the robustness of the proposed elements and different constitutive linearizations. An in-scale laboratory test on the collapse of a masonry arch bridge will also be arranged for the benchmark purpose. On the other hand, an investigation of the different modeling of the backfill will be conducted. In particular, we will study the effect of assuming different dilation angles for the backfill material. The possibility of introducing the auto re-meshing procedure for the backfill region will also be studied to speed up the analysis.

CRediT authorship contribution statement

Yiwei Hua: Writing – review & editing, Writing – original draft, Visualization, Validation, Software, Methodology, Investigation, Funding acquisition, Conceptualization. **Gabriele Milani:** Writing – review & editing, Conceptualization, Methodology, Supervision.

Declaration of competing interest

The authors declare that they have no known competing financial interests or personal relationships that could have appeared to influence the work reported in this paper.

Data availability

Data will be made available on request.

Acknowledgments

Yiwei Hua would like to thank the financial support from China Scholarship Council (CSC) under the grant CSC No. 202108320019.

References

[1] Franck SA, Bretschneider N, Slowik V. Safety analysis of existing masonry arch bridges by nonlinear finite element simulations. Int J Damage Mech 2020;29:126–43. https://doi.org/10.1177/1056789519865995.
[2] Conde B, Díaz-Vilariño L, Lagüela S, Arias P. Structural analysis of Monforte de Lemos masonry arch bridge considering the influence of the geometry of the arches and fill material on the collapse load estimation. Constr Build Mater 2016;120:630–42. https://doi.org/10.1016/j.conbuildmat.2016.05.107.
[3] Portioli FPA. Rigid block modelling of historic masonry structures using mathematical programming: a unified formulation for non-linear time history, static pushover and limit equilibrium analysis. Bull Earthq Eng 2020;18:211–39. https://doi.org/10.1007/s10518-019-00722-0.
[4] Stockdale G, Milani G. A comprehensive analysis structure for the design of masonry arches. Open Civ Eng J 2022;15:381–97. https://doi.org/10.2174/1874149502115010381.
[5] Iannuzzo A, Dell'Endice A, Van Mele T, Block P. Numerical limit analysis-based modelling of masonry structures subjected to large displacements. Comput Struct 2021;242:106372. https://doi.org/10.1016/j.compstruc.2020.106372.
[6] Livesley RK. A computational model for the limit analysis of three-dimensional masonry structures. Meccanica 1992;27:161–72. https://doi.org/10.1007/BF00430042.
[7] Milani G, Lourenço PB. 3D non-linear behavior of masonry arch bridges. Comput Struct 2012;110–111:133–50. https://doi.org/10.1016/j.compstruc.2012.07.008.
[8] Krabbenhoft K, Lyamin AV, Hjiaj M, Sloan SW. A new discontinuous upper bound limit analysis formulation. Int J Numer Methods Eng 2005;63:1069–88. https://doi.org/10.1002/nme.1314.
[9] Krabbenhøft K, Lyamin AV, Sloan SW. Three-dimensional Mohr-Coulomb limit analysis using semidefinite programming. Commun Numer Methods Eng 2008;24:1107–19. https://doi.org/10.1002/cnm.1018.
[10] Li P-Y, Dou H-Q, Nie W-F. Stability analysis of geosynthetic-reinforced slopes considering multiple potential failure mechanisms based on the upper bound theorem. Int J Geomech 2024;24. https://doi.org/10.1061/IJGNAI.GMENG-8428.
[11] Jin Z, Zhang C, Li W, Tu S, Wang L, Wang S. Stability analysis for excavation in frictional soils based on upper bound method. Comput Geotech 2024;165. https://doi.org/10.1016/j.compgeo.2023.105916.
[12] Tschuchnigg F, Schweiger HF, Sloan SW. Slope stability analysis by means of finite element limit analysis and finite element strength reduction techniques. Part II: Back analyses of a case history. Comput Geotech 2015;70:178–89. https://doi.org/10.1016/j.compgeo.2015.07.019.
[13] Cavicchi A, Gambarotta L. Collapse analysis of masonry bridges taking into account arch-fill interaction. Eng Struct 2005;27:605–15. https://doi.org/10.1016/j.engstruct.2004.12.002.
[14] Cavicchi A, Gambarotta L. Two-dimensional finite element upper bound limit analysis of masonry bridges. Comput Struct 2006;84:2316–28. https://doi.org/10.1016/j.compstruc.2006.08.048.
[15] Wan HL, Lam CC. Parametric Study of In-Plane Collapse Mechanism of Panels with Different Masonry Geometric Bond Patterns. In: Endo Y, Hanazato T, editors. Struct Anal Hist Constr SAHC 2023 RILEM Bookseries, Vol 46. Cham: Springer; 2024. p. 556–65. https://doi.org/10.1007/978-3-031-39450-8_46.
[16] Wang Q, dos Santos KRM, Beyer K. Micro modeling of irregular stone masonry walls using mathematical programming. In: Endo Y, Hanazato T, editors. Struct Anal Hist Constr SAHC 2023 RILEM Bookseries, Vol 46. Cham: Springer; 2024. p. 591–602. https://doi.org/10.1007/978-3-031-39450-8_49.
[17] Gagliardo R, Cascini L, Portioli F, Landolfo R. Blind-test numerical simulation of shake-table tests on three-leaf masonry walls: an application of LIA block_3D. In: COMPDYN Proc; 2019. p. 4699–706. https://doi.org/10.7712/120119.7261.19695.
[18] Grillanda N, Chiozzi A, Milani G, Tralli A. Tilting plane tests for the ultimate shear capacity evaluation of perforated dry joint masonry panels. Part II: Numerical analyses. Eng Struct 2020:111460. https://doi.org/10.1016/j.engstruct.2020.111460.
[19] Wang P, Milani G. Specialized 3D Distinct element limit analysis approach for a fast seismic vulnerability evaluation of massive masonry structures: Application on traditional pagodas. Eng Struct 2023;282. https://doi.org/10.1016/j.engstruct.2023.115792.
[20] Valentino J, Gilbert M, Gueguin M, Smith CC. Limit analysis of masonry walls using discontinuity layout optimization and homogenization. Int J Numer Methods Eng 2023;124:358–81. https://doi.org/10.1002/nme.7124.
[21] Gilbert M, Casapulla C, Ahmed HM. Limit analysis of masonry block structures with non-associative frictional joints using linear programming. Comput Struct 2006;84:873–87. https://doi.org/10.1016/j.compstruc.2006.02.005.
[22] Gilbert M, Nguyen D, Smith C. Computational limit analysis of soil-arch interaction in masonry arch bridges. In: Proc 5th int conf arch bridg ARCH; 2007. pp. 633–640. http://www.civil.uminho.pt/masonry/Publications/ARCH07/647_654.pdf.
[23] Sloan SW, Kleeman PW. Upper bound limit analysis using discontinuous velocity fields. Comput Methods Appl Mech Eng 1995;127:293–314. https://doi.org/10.1016/0045-7825(95)00868-1.
[24] Sloan SW. Lower bound limit analysis using finite elements and linear programming. Int J Numer Anal Methods Geomech 1988;12:61–77. https://doi.org/10.1002/nag.1610120105.
[25] Ferris MC, Tin-Loi F. Limit analysis of frictional block assemblies as a mathematical program with complementarity constraints. Int J Mech Sci 2001;43:209–24. https://doi.org/10.1016/S0020-7403(99)00111-3.
[26] Fishwick RJ. Limit analysis of rigid block structures. University of Portsmouth 1996. https://doi.org/10.1007/978-1-349-95810-8_1241.
[27] Maier G, Nappi A. A theory of no-tension discretized structural systems. Eng Struct 1990;12:227–34. https://doi.org/10.1016/0141-0296(90)90021-J.
[28] Hua Y, Milani G. Simple modeling of reinforced masonry arches for associated and non-associated heterogeneous limit analysis. Comput Struct 2023;280. https://doi.org/10.1016/j.compstruc.2023.106987.
[29] Heyman J. The safety of masonry arches. In: Mason. Bridg. Viaducts Aqueducts; 2017. p. 329–52. doi: 10.4324/9781315249513-20.
[30] Heyman J. The stone skeleton. Int J Solids Struct 1966; 2: 249–256. IN1–IN4, 257–264, IN5–IN12, 265–279. doi: 10.1016/0020-7683(66)90018-7.
[31] Drucker DC. Coulomb friction, plasticity, and limit loads. J Appl Mech 1954;21:71–4. https://doi.org/10.1115/1.4010821.
[32] Bottero A, Negre R, Pastor J, Turgeman S. Finite element method and limit analysis theory for soil mechanics problems. Comput Methods Appl Mech Eng 1980;22:131–49. https://doi.org/10.1016/0045-7825(80)90055-9.
[33] Engwirda D. Locally-optimal Delaunay-refinement and optimisation-based mesh generation. University of Sydney; 2014.
[34] Page J. Load tests to collapse on two arch bridges at preston, shropshire and prestwood, Staffordshire. Res Rep - Transp Road Res Lab; 1987.
[35] Betti M, Drosopoulos GA, Stavroulakis GE. Two non-linear finite element models developed for the assessment of failure of masonry arches. Comptes Rendus - Mec 2008;336:42–53. https://doi.org/10.1016/j.crme.2007.10.014.
[36] Drosopoulos GA, Stavroulakis GE, Massalas CV. Limit analysis of a single span masonry bridge with unilateral frictional contact interfaces. Eng Struct 2006;28:1864–73. https://doi.org/10.1016/j.engstruct.2006.03.016.